

# The TIME Table: Rotation and Ages of Cool Exoplanet Host Stars

Eric Gaidos<sup>★1,2,3</sup>, Zachary Claytor<sup>4,5</sup>, Ryan Dungee<sup>6</sup>, Aleezah Ali<sup>4</sup>, Gregory A. Feiden<sup>7</sup>

<sup>1</sup>Department of Earth Sciences, University of Hawai'i at Mānoa, Honolulu, HI 96822, USA

<sup>2</sup>Institute for Astronomy, University of Vienna, 1180 Wien, Austria

<sup>3</sup>Institute for Particle Physics & Astrophysics, ETH Zürich, 8093 Zürich, Switzerland

<sup>4</sup>Institute for Astronomy, University of Hawai'i at Mānoa, Honolulu, HI 96822 USA

<sup>5</sup>Department of Astronomy, University of Florida, 211 Bryant Space Science Center, Gainesville, FL 32611 USA

<sup>6</sup>Institute for Astronomy, University of Hawai'i at Hilo, Hilo, HI 96720 USA

<sup>7</sup>Department of Physics and Astronomy, University of North Georgia, Dahlonega, GA 30597 USA

Submitted, accepted

## ABSTRACT

Age is a stellar parameter that is both fundamental and difficult to determine. Among middle-aged M dwarfs, the most prolific hosts of close-in and detectable exoplanets, gyrochronology is the most promising method to assign ages, but requires calibration by rotation-temperature sequences (gyrochrones) in clusters of known ages. We curated a catalog of 249 late K- and M-type ( $T_{\text{eff}}=3200\text{--}4200\text{K}$ ) exoplanet host stars with established rotation periods, and applied empirical, temperature-dependent rotation-age relations based on relevant published gyrochrones, including one derived from observations of the 4 Gyr-old open cluster M67. We estimated ages for 227 of these stars, and upper limits for 8 others, excluding 14 which are too rapidly rotating or are otherwise outside the valid parameter range of our gyrochronology. We estimated uncertainties based on observed scatter in rotation periods in young clusters, error in the gyrochrones, and uncertainties in temperature and non-solar metallicity. For those stars with measured metallicities, we provide but do not incorporate a correction for the effects of deviation from solar-metallicity. The age distribution of our sample declines to near zero at 10 Gyr, the age of the Galactic disk, with the handful of outliers explainable by large uncertainties. Continued addition or extension of cluster rotation sequences to more thoroughly calibrate the gyrochronology in time and temperature space, more precise and robust measurement of rotation periods, and more accurate stellar parameter measurements will enable continued improvements in the age estimates of these important exoplanet host stars.

**Key words:** exoplanets – stars: evolution – stars: late-type – stars: low-mass – stars: rotation – planetary systems

## 1 INTRODUCTION

Over the past three decades, thousands of planets have been discovered around other stars. Exoplanet surveys have revealed that M-type dwarfs, the least massive but most numerous stars, host more planets on close-orbits than their solar-mass counterparts (Mulders et al. 2015; Hardegree-Ullman et al. 2019; Hsu et al. 2019). These include Earth-size, rocky planets that orbit within the compact habitable zone of these intrinsically faint stars, and which are more feasible to study, e.g. with *JWST*, because of the host stars' lower mass, radius, and luminosity.

Precise characterization of the host star (e.g., radius, mass, luminosity, metallicity) is essential to obtain properties of its planets, but is challenging for very low-mass stars for which methods tuned to the Sun do not apply. For this reason, empirical approaches

have proven useful for M dwarfs, enabled by the advent of the *Gaia* astrometry mission, space- and ground-based photometric surveys, and advances and expansion in spectroscopic instrumentation. For example, interferometry can directly measure the angular radii of very nearby M dwarfs; pairing with trigonometric parallaxes yields physical radii. Combined with a bolometric luminosity from a flux-calibrated spectral energy distribution (SED), this allows the effective temperature  $T_{\text{eff}}$  to be derived using the Stefan-Boltzmann law (Boyajian et al. 2012). Spectra of stars with a range of established  $T_{\text{eff}}$  can then serve as templates to estimate the  $T_{\text{eff}}$  of more distant stars using spectra and, combining with SEDs, their radii (Mann et al. 2015). Metallicities can be calibrated using binaries where the solar-type companion has an established metallicity (relative to the Sun) (e.g., Mann et al. 2013, 2014; Montes et al. 2018; Souto et al. 2020).

Age is a fundamental property of planets but is difficult to accurately estimate for most systems (Christensen-Dalsgaard & Aguirre

★ Contact e-mail: gaidos@hawaii.edu

2018). Planets and their atmospheres are expected to evolve under the influence of their host star and their own internal thermodynamics and compositional change (Kite et al. 2009; Lammer 2013). For temperate, Earth-like planets, changes in atmospheric composition will be the backdrop against which biosignatures will be searched for. Observations of disk lifetimes, planet formation theory, and isotope-ages of Solar System bodies indicate that the age of a star should be no more than a few tens of Myr older than that of its planets (Helled & Morbidelli 2021), but ages of most host stars remain poorly constrained. Planets are difficult to detect around young stars (e.g., Miyakawa et al. 2022) and most planet hosts are older and no longer members of (relatively) well-dated clusters and young-moving groups.

Ages of isolated field stars have been estimated by (1) comparison of stellar parameters to stellar models (e.g., in a color-magnitude diagram); (2) asteroseismic measurement of increasing density due to the conversion of H into He and heavy elements in stellar interiors; (3) the abundance of lithium, which is destroyed in stellar interiors; (4) metallicity and the overall age-metallicity relation of the Galactic disk; (5) increase in the peculiar motion of stars with time with respect to the overall orbital motion of the Galactic disk as a result of perturbations from molecular clouds and other stars; and (6) rotation and rotation-driven magnetic activity that decline as angular momentum (AM) is lost through a magnetized wind.

But M dwarfs are resistant to most age-dating techniques: They evolve imperceptibly on the main sequence (MS; Adams et al. 2005) and the pulsations that are the grist of asteroseismology are below current detection thresholds (Rodríguez-López 2019, and regardless the stars' densities do not change). M dwarfs consume their lithium within  $\sim$ 50 million years (Binks & Jeffries 2014) and thus this proxy cannot be used at later ages, and metallicity and peculiar motions are only meaningful in a statistical sense for stellar populations, not individual stars; the age-metallicity relation appears flat for disk stars (Rebassa-Mansergas et al. 2021) and age-abundance ratio relations do not appear to apply universally (Casali et al. 2020).

This leaves gyrochronology, the application of relations between age and rotation (and its proxies) brought about by stellar spin-down, as a viable method to age-date main-sequence M dwarfs in the field (Barnes 2007). Such stars are potentially well-suited for this approach because they have a smaller or no inner radiative core which can rotate quasi-independently of the convective envelope, and instead could have behavior similar to simple “solid-body” rotation. However, spin-down driven by magnetic activity scales with the Rossby number  $Ro \equiv P_{\text{rot}}/\tau_c$ , where  $\tau_c$  is the local turnover time in the convective envelope, and the longer  $\tau_c$  of M dwarfs compared to solar-type stars means their rotational evolution will be distinct. Using co-eval bairries, Otani et al. (2022) tested several color-dependent spin-down models for internal consistency, and derived *internal* errors (i.e., only those arising from errors in  $P_{\text{rot}}$  and color) of 5-10% for relatively young early M-type stars.

Pioneering ground-based observations of open clusters of co-eval stars, followed by the revolutionary wide-field surveys of the *Kepler* and *TESS* space telescopes, document the formation of tight sequences in rotation vs. color or  $T_{\text{eff}}$  diagrams that extend to cooler temperatures and longer  $\tau_c$  with time (Gallet & Bouvier 2015; Curtis et al. 2020). The formation of the sequence among solar-mass stars is thought to be the result of a change in the braking law (i.e., the rotation-rate dependence of the torque) as stars transition from a “saturated” (less rotation rate-dependent) phase to an “unsaturated” (more rotation rate-dependent) phase of stellar activity at a critical value of  $Ro$  (Matt et al. 2012; Curtis et al. 2019a). After a star enters this regime the strong rotation rate dependence effectively erases the

effect of initial conditions, allowing gyrochronologic relations to be applied.

Among cooler dwarf stars the situation is more complex. The outer convective envelope—the part of the star that is both observable and feels the decelerating torque from the magnetized wind—is more substantial, and the coupling timescale between the envelope and the radiative core is longer. Among K dwarfs, this can lead to early differential rotation, with the core spinning faster than the envelope, and later “stalling” as the core transfers AM to the envelope and the observed spin-down temporarily slows or halts (Denissenkov et al. 2010; Curtis et al. 2019b, 2020). Stalling could contribute to the formation of a rotational sequence, but also delays the epoch at which gyrochronology is useful. Among yet cooler M dwarfs the radiative core is smaller or absent, the coupling timescale is expected to get longer, and the magnitude of the stalling could diminish/disappear (Lu et al. 2022).

The mechanism responsible for core-envelope coupling has not been established, nor has a theoretical model that is quantitatively consistent with the observations and has predictive power over a range of  $T_{\text{eff}}$  been constructed. Moreover, it is not certain if braking laws developed for solar-type stars apply to M dwarfs. For these reasons, observations of stars in clusters of known ages are imperative for identifying rotational sequences (vs.  $T_{\text{eff}}$ ), constructing empirical rotation-age relations, and calibrating successful models. But M dwarfs are intrinsically faint and their rotation evolves more slowly, and thus deeper observations of older (and statistically more distant) clusters are required. M dwarfs in these clusters are beyond the range of current space telescopes both in terms of signal (limited by the modest telescope aperture) and spatial resolution (limited by the large pixel size). *K2* monitoring of the oldest nearby cluster (Ruprecht 147,  $\approx$ 2.7 Gyr; Curtis et al. 2013) captured rotation periods for only a handful of M dwarfs near the K-M boundary. Similar observations of the nearest old cluster (M67,  $\approx$ 4 Gyr Richer et al. 1998; Vandenberg & Stetson 2004; Schiavon et al. 2004; Sarajedini et al. 2009) failed to yield useful results (Eselstein et al. 2018).

Ground-based observatories can go deeper and with high resolution. Dungee et al. (2022) carried out a Sloan *i*-band monitoring campaign of late K and early M dwarf members of M67 with the MegaCAM wide-field camera at the prime focus of the 3.6-m Canada France Hawaii Telescope (CFHT) (Boulade 1998), obtaining 294 rotation periods and identifying a rotational sequence that ranged from  $\approx$ 25 days at 4200K to 125 days at 3200K. Dungee et al. (2022) found that the “warm” end of the M67 sequence could be explained by the overlapping “cool” end of the Ruprecht 147 sequence identified by Curtis et al. (2020), plus Skumanich-like power-law spin-down  $P \propto t^n$  Skumanich (1972) with an index  $n = 0.62$ . This indicates that (a) the rotation sequence of M dwarfs extends close to the fully convective boundary (near  $T_{\text{eff}}=3200\text{K}$ ) by no later than 4 Gyr; (b) spin-down among middle-aged M dwarfs seems to obey a relatively simple braking law. Both of these findings bode well for the gyrochronology of very cool dwarfs.

In this work, we curate a catalog of rotation periods of late K and early M-type dwarfs known to host validated or confirmed planets<sup>1</sup>, and apply empirical rotation-age relations based on the M67 gyrochrone of Dungee et al. (2022) and previously published gyrochrones (Curtis et al. 2020) to estimate ages. The rotation periods of many host stars have been established either using the

<sup>1</sup> A “validated” planet is one for which known false positive scenarios are highly unlikely; a “confirmed” planet has been detected by a second, independent method.

same space-based photometry (i.e., *Kepler*, *K2*, *TESS*) used to identify their transiting planets, or by data obtained from the ground- or space as part of the validation/confirmation of candidate planets. There are also collections of rotation periods of field stars (including planet hosts) based on data from *Kepler* (Santos et al. 2019, 2021), *K2* (Reinhold & Hekker 2020), *TESS* (Canto Martins et al. 2020), and ground-based surveys (Oelkers et al. 2018; Newton et al. 2018; Christy et al. 2022). We also identify additional candidate rotational signatures directly in the photometric datasets. We emphasize that some rotation periods are tentative and that very cool dwarf gyrochronology is a work in progress and makes assumptions which will be borne out or refuted by future observations.

## 2 SOURCES OF ROTATION PERIODS

We identified all host stars of validated or confirmed exoplanets with  $T_{\text{eff}}$  of 3200–4200 K in the NASA Exoplanet Archive as of August 2022. This included 112 *Kepler* host stars or *Kepler* Objects of Interest (KOIs) having rotation periods  $P_{\text{rot}}$  in Santos et al. (2019). From the list of the non-*Kepler* host stars we removed evolved (giant), T Tauri, and pre-main sequence (PMS) stars, as rotation of these stars obviously does not follow the gyrochronology of dwarfs, as well as members of star-forming regions and young moving groups that have ages estimated by other techniques, leaving 215 non-*Kepler* stars.

Rotation periods for these stars were obtained from the literature; these were determined using ground- or space-based photometry, e.g. by WASP (Pollacco et al. 2006), MEarth (Berta et al. 2012), ASAS-SN (Shappee et al. 2014), *K2* (Howell et al. 2014), and *TESS* (Ricker et al. 2014) and/or time-series spectroscopy of indicators of active regions and magnetic fields, notably by the HARPS (Pepe et al. 2000) and CARMENES Doppler RV surveys for exoplanets (Reiners et al. 2018).

We revisited the *K2* data by matching all stars against the EPIC catalog (Huber et al. 2016) and downloaded all Pre-search Data Conditioning Simple Aperture Photometry (PDCSAP) lightcurves from the MAST archive (including many *K2*-detected transiting exoplanet host stars). The lightcurves were further de-trended with a best-fit second-order polynomial before a Lomb-Scargle analysis (Scargle 1982) to search for signals with periods of 0.4–40 days, an interval chosen to avoid the pervasive 6-hr thruster firing signal and for the typical lightcurve to span at least two periods. 115 lightcurves of 95 EPIC stars contained peaks exceeding a  $p = 0.001$  false-positive level. Of these 20 were not previously published, and in one other case (*K2*-345) we replaced the Reinhold & Hekker (2020) value as being obviously erroneous. We did not revise other Reinhold & Hekker (2020) values. In 11 cases (*K2*-5, 14, 83, 124, 125, 129, 151, 288B, 315, 322, 377) we judged that the peak was an upper harmonic and doubled the period and its error based on inspection of the lightcurve. The de-trended lightcurves and periodograms are shown in Figs. A1–A4.

We retrieved lightcurves from the Zwicky Transient Facility (ZTF, Masci et al. 2019) using the Python wrapper of the InfraRed Science Archive (IRSA) API query (Rigault 2018) and a matching criteria of 5''. We obtained 319 ZTF lightcurves for 102 stars; each star has up to three (*gri*) lightcurves and sometimes the 5'' search cone contained more than one star. We constructed Lomb-Scargle periodograms of the 145 lightcurves with at least 100 points (the maximum was 1092) and identified 25 signals among 22 stars with peaks with a false alarm probability  $< 0.01$ . (We were less stringent than for *K2* because of the availability of data in multiple filters for

comparison). For three stars with two periodic signals (in different filters), none had matching periods. Seven signals were rejected based on similarity to the lunar synodic period (29.5 day) or its seasonal alias (27.3 and 32.1 days). Marginal, long term ( $> 100$ -day) signals seen in the lightcurves of *K2*-123 and *K2*-124 were rejected based on detection of shorter rotation periods by *K2*. ZTF periods for two other systems (TOIs-2136 and 3174) were already reported in the literature. We assigned tentative periods to four other stars based on these data; none of these periods are close to the 29.5-day lunar synodic period or its annual alias, or harmonics of 1-day (Fig. A5). All other periodograms contained no clearly visible peaks or a forest of peaks of roughly equal (in)significance. We also retrieved *g*- and *V*-band lightcurves from the All-Sky Automated Search for Super-Novae (ASAS-SN Shappee et al. 2014; Kochanek et al. 2017) on which we performed a similar analysis. We identified 16 and 15 host stars with significant ( $p < 0.01$ ) periodic signals in the *g*- and *V*-band data, respectively. Among these are four stars that have matching *g*- and *V*-band periods that are not at the lunar synodic period, its aliases, or 1-day harmonics. The *g*-band photometry for these is shown in Fig. A6. In the case of GJ 486, the detected signals at 13.7 days differ markedly from the published  $P_{\text{rot}}$  of  $49.9 \pm 5.5$  days (Caballero et al. 2022) (which we retain).

We included  $P_{\text{rot}}$  values determined from time-series measurements of spectroscopic indicators of stellar activity such as Ca II HK and H $\alpha$ , but we excluded estimates based on correlations with indicators of stellar activity, e.g., the overall level of Ca II HK emission (e.g., Astudillo-Defru et al. 2017b).

## 3 STELLAR PARAMETERS

We retrieved values for  $T_{\text{eff}}$  and metallicities ([Fe/H]) of KOIs from the literature via the NASA Exoplanet Archive tables (Thompson et al. 2018; Coughlin et al. 2016; Mullally et al. 2015; Rowe et al. 2015; Burke et al. 2014; Batalha et al. 2013). For each star, we used the most recent KOI table available. However, the present characterization of cool exoplanet host stars is markedly heterogeneous, with many stars lacking published metallicities, and multiple values for the same star can differ by much more than the published uncertainties. For those stars without effective temperature solutions from the NASA Exoplanet Archive, we used their absolute  $K_s$  magnitude to calculate an effective temperature with the Mann et al. (2015) empirical relations.

We identified stars in multiple systems using the literature, as well as stars with *Gaia* astrometric renormalized unit weight error (RUWE) values  $> 1.4$  indicative of unresolved multiplicity (Belokurov et al. 2020). We flagged but did not exclude these systems, cautioning that binaries that are unresolved in the data used to obtain rotational signals could be assigned incorrect rotation periods, and a single-star gyrochronology is expected to be more erroneous or fail in sufficiently close binaries (see Section 7.1).

We searched for additional, unpublished stellar companions resolved by *Gaia* (separations  $\gtrsim 1''$ ) and identifiable based on similar parallaxes and proper motions in the DR3 catalog (Gaia Collaboration et al. 2016, 2022). This was performed by calculating a Bayesian probability that a candidate companion's astrometry is the same as a given star, relative to the probability that this occurs in a "background" population. We identified five stars with  $\text{FAP} < 0.01$ , but all are previously known binaries.

We searched the *Hipparcos-Gaia* (EDR3) Catalog of Accelerations (Brandt 2021) and found 5 matches, a paucity that reflects the magnitude limit of the *Hipparcos* catalog. Of these, only two

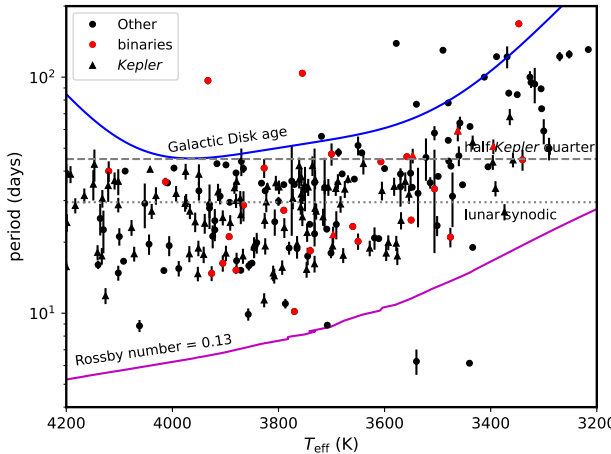


**Figure 1.** Rotation periods of late-K and early M-type hosts of known exoplanets from the literature and this work. Members of multi-star systems are indicated in red. The horizontal dashed and dotted lines mark one half the *Kepler* rotation interval (close to one half the *K2* campaign interval) and the lunar synodic period, near which ground-based detection of  $P_{\text{rot}}$  values are limited. The magenta curve is the  $P_{\text{rot}}$  above which a star's Rossby number exceeds the critical value (based on convective turnover times from the Dartmouth magnetic model) and activity leaves the “saturated” phase, and the blue curve is the  $P_{\text{rot}}$  predicted for stars with the age of the Galactic disk using the [Dungee et al. \(2022\)](#) gyrochrones and power-law evolution. Errors in  $T_{\text{eff}}$  are not shown but are typically 75K.

have  $\chi^2$  fits approaching but not reaching a formal 0.3% false-alarm probability threshold of 11.8: HD 238090 ( $\chi^2 = 9.1$ ) is the primary of a mid-M-type companion at 14.6'' (224 au) that is unlikely to be the source of any acceleration, and HIP 71135 ( $\chi^2 = 9.3$ ) which has no known stellar companion. The RV-detected planets are inferred to have (sub)-Neptune-like masses ([Feng et al. 2019](#); [Stock et al. 2020](#)), and could not produce detectable acceleration. Finally, we searched the catalog of the Robo-AO M-dwarf Multiplicity Survey ([Lamman et al. 2020](#)), which identified candidate companions with separations of 0.1-4'' of nearby M dwarfs from the [Lépine & Shara \(2005\)](#) catalog. We identified 20 overlapping stars, none of which had AO-identified companions.

Figure 1 plots  $P_{\text{rot}}$  vs.  $T_{\text{eff}}$  for the catalog of host stars, with *Kepler*- and non-*Kepler* hosts marked by different points and members of known binaries shown in red. The horizontal dashed line marks 90 days, the cadence at which *Kepler* performed a role maneuver that introduced systematics in lightcurves, only slightly longer than the 80-day interval which the spacecraft could observe a field during the *K2* mission. Recovery of rotation periods longer than these intervals is inhibited by these systematics. The horizontal dotted line is the lunar synodic period of 29.5 days near which the ground-based detection of rotation periods is inhibited. The magenta curve is the critical  $P_{\text{rot}}$  at which  $Ro = 0.13$  using the [Jeffries et al. \(2011\)](#) prescription for  $\tau_c$ . Nearly all stars are above this line and are thus in the “unsaturated” regime of dynamo-driven activity, although not necessarily yet in Skumanich-like spin-down. The blue curve is the expected  $P_{\text{rot}}$  for 10 Gyr, the approximate age of the Galactic disk ([Kilic et al. 2017](#), but see [Xiang & Rix \(2022\)](#)).

#### 4 AGE ESTIMATION

We estimated the age of each star with an established  $P_{\text{rot}}$  (Sec. 2) by comparing it to available empirical cluster gyrochrones that (partially) include the  $T_{\text{eff}}$  range of interest, i.e., that of M67 [Dungee et al. \(2022\)](#), but also that of the 2.7 Gyr-old Ruprecht 147 ([Curtis et al. 2020](#)), the 1.4 Gyr-old NGC 752 ([Agüeros et al. 2018](#)), the 1 Gyr-old NGC 6811 ([Curtis et al. 2019a](#)), and the 0.67 Gyr-old Praesepe ([Douglas et al. 2019](#)), as filtered for binaries and fit with polynomials by [Curtis et al. \(2020\)](#).

[Dungee et al. \(2022\)](#) fit the M67 rotation sequence with a fourth-order polynomial with  $T_{\text{eff}}$  over 3200-4200K.

$$P_{\text{Gyr}} = 9.66 \times 10^{-10} \cdot (T_{\text{eff}} - 4000)^4 + 8.25 \times 10^{-7} \cdot (T_{\text{eff}} - 4000)^3 + 2.69 \times 10^{-4} \cdot (T_{\text{eff}} - 4000)^2 + 0.016 \cdot (T_{\text{eff}} - 4000) + 25.9, \quad (1)$$

$T_{\text{eff}}$  of M67 members were estimated from their Pan-STARRS  $r - i$  colors using a polynomial relation based on synthetic photometry of nearby M dwarf standards ([Mann et al. 2015](#)). [Curtis et al. \(2020\)](#) fit the other rotational sequences as polynomials with *Gaia*  $B_P - R_P$  color (see their Appendix B), which we converted to  $T_{\text{eff}}$  using the empirical MS of [Pecaut & Mamajek \(2013\)](#).

We estimated ages by simple power-law interpolation between gyrochrones calibration points (linear interpolation in a log-log plot of period vs. age). Calibration points were calculated from Eqn. 1 and [Curtis et al. \(2020\)](#) for a given stellar  $T_{\text{eff}}$ . Figure 2 plots the derived period vs. age tracks for a range of representative  $T_{\text{eff}}$ . The flattening of the tracks at ages younger than Ruprecht 147 could be “stalling” of spin-down as a faster rotating radiative core adds AM to the convective envelope ([Curtis et al. 2020](#)) (see Sec. 7.1). The bunching of the hotter tracks reflects the weak dependence of  $P_{\text{rot}}$  on  $T_{\text{eff}}$  among co-eval K dwarfs ([Curtis et al. 2020](#)).

A calibration point was used only if (1)  $T_{\text{eff}}$  falls within the range of a gyrochrones; (2) for the particular  $T_{\text{eff}}$  and gyrochrones rotation period, the star would not be in the “saturated” phase of activity (a condition for a rotational sequence); and (3) the star would not be on the PMS and still affected by contraction and spin-up at that gyrochrones age. The condition for saturated activity is a Rossby number  $Ro = P_{\text{rot}}/\tau_c$  where  $\tau_c$  is the local convective turnover time, to be less than a critical value. We adopted the relation of  $\tau_c$  with luminosity of [Jeffries et al. \(2011\)](#) and critical  $Ro$  of 0.13 ([Wright et al. 2018](#)). PMS durations were taken from the Dartmouth standard models of stellar evolution ([Dotter et al. 2008](#)).

If the only available calibration point was that of M67 (4 Gyr) then we calculate the age of the star using the Skumanich-like spin-down law that [Dungee et al. \(2022\)](#) found by comparing the rotational sequence of M67 with that of 2.7 Gyr-old Ruprecht 147 ([Curtis et al. 2020](#))

$$t = t_0 (P/P_0)^{1/n}, \quad (2)$$

with  $n = 0.62$ . However, if the age derived in this manner was  $< 2.7$  Gyr (i.e., that of Ruprecht 147) we took this to be an upper limit. If additional calibration points were available we derived an age as above; if that was  $< 4$  Gyr we then consequently derived ages by power-law interpolation between successfully younger pairs of neighboring calibration points until the derived age lay between the ages of the gyrochrones. However, if the age determined from the 4 Gyr and next youngest calibration points was  $> 4$  Gyr, we adopted that age. This allowed for the occasional pathological cases where the [Dungee et al. \(2022\)](#) gyrochrones produced an age that was slightly  $< 4$  Gyr, but the gyrochrones pair produced an age slightly  $> 4$  Gyr. If no self-consistent age was produced (i.e., the age was

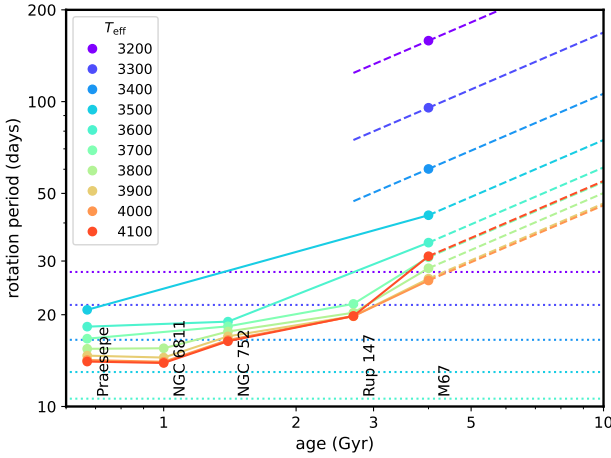


**Figure 2.** Rotation period vs. age tracks constructed from five cluster gyrochrones (vertically labelled). The dashed parts of the trajectory are based on the Skumanich-like relation derived by [Dungee et al. \(2022\)](#), with extrapolation beyond 4 Gyr. Dotted lines are the periods above which the Rossby number exceeds the critical value for unsaturated activity ( $\approx 0.13$ ) at each  $T_{\text{eff}}$ .

younger than the youngest calibration point) we adopted the age of the youngest valid gyrochrone as an upper limit.

Monte Carlo (MC) realizations of these calculations were performed to estimate the uncertainty in the age, incorporating error in rotation period, stellar parameters, the gyrochronology, and initial conditions (see Sec. 5). The mean and standard error of the age distributions were adopted as the nominal age and its uncertainty reported in Table 6. If the MC realizations produced only upper limits, the 95 percentile value of the distribution was reported as an upper limit. If neither values nor upper limits were produced, or the resulting age would place the star on the PMS, no age was assigned.

## 5 AGE ERROR ANALYSIS

Error in gyrochronologic age assignment arises from (1) the formal uncertainty in  $P_{\text{rot}}$ , as well as systematic errors in  $P_{\text{rot}}$  not included in the formal error (i.e., aliasing and confusion with harmonics); (2) the formal error in the gyrochrones as well as uncertainty in the ages of the calibrator clusters; (3) errors in  $T_{\text{eff}}$  used to apply the calibration; (4) variation in initial conditions, i.e. the angular momentum or rotation rate at an early time; and (5) stellar rotational evolution that deviates from the assumed behavior due to differences in the internal structure of a star or the wind torque.

[Epstein & Pinsonneault \(2014\)](#) quantified the effect of uncertainty in  $P_{\text{rot}}$  (#1 above) and scatter in rotation period at a fixed age (#4) by projecting “initial” rotation conditions found in the  $\sim 500$  Myr-old cluster M37 forward in time with a rotational model. They found that the age uncertainty among middle-aged M dwarf stars is very large, dominated by the scatter in initial conditions, and as a result the age precision is very poor (factors of two or more between minimum and maximum ages) because, essentially, these stars have not yet spun down to form a rotational sequence, but this depends on the details of the model, including the assumed braking law.

Here we use Monte Carlo methods to calculate probabilistic distributions of ages — an approach used by [Otani et al. \(2022\)](#) — and take the standard deviation as the error. Where data are available

we determine variation empirically; otherwise we rely on models of stellar interior and rotational evolution.

### 5.1 Period Error

We report and use the formal uncertainties in rotation period either from the literature, or from our periodogram analysis. In the latter case, Gaussian functions are set to the periodogram peak and the standard deviation is taken to be the Gaussian width  $\sigma$ . This uncertainty can arise from the finite observation baseline relative to the rotation period, particularly for older stars with longer rotation periods. Significant evolution in the spots causing rotational variability can occur over a few rotation periods ([Basri et al. 2022](#)), causing drift in the phase of the overall photometric signal and broadening of the peak. Differential rotation, combined with changes in the latitude of spots, will also broaden a periodogram peak or even produce distinct neighboring peaks (e.g., [Reinhold et al. 2013](#); [Balona & Abedigamba 2016](#)).

The first (upper) harmonic might be confused for the true period as a result of the distribution of star-spots (e.g., [Suto et al. 2022](#)), causing the star to appear much younger than it is. Ground-based observations may incur much larger systematic error as a result of aliasing caused by sampling bias on nocturnal, lunar synodic, or seasonal timescales. This can distribute the power in single periodic signal into multiple weaker peaks in a periodogram ([VanderPlas 2018](#)). These peaks can either be “failure modes” if the peak is far from the true period, or if close to the true period and unresolved due to limiting sampling, broaden the peak and resulting uncertainty. Given the diverse data sets and sources, we point out but do not attempt to quantify such errors in this work.

### 5.2 Gyrochrone error

Due to finite sample size and error in  $T_{\text{eff}}$  and  $P_{\text{rot}}$ , the gyrochrones themselves have uncertainties. These are not typically published, but since most of the ages in TIME-Table rely heavily on the 4 Gyr-old M67 gyrochrone, we determined uncertainties in the best-fit polynomial coefficients using Monte-Carlo simulations. This is shown as the dashed black lines in Fig. 3. The ages of the clusters used to calibrate the gyrochronology themselves have significant standard errors and systematics; full consideration of these is beyond the scope of this work but should be included when considering rotation-based ages in an absolute sense ([Sandquist et al. 2021](#)).

### 5.3 Error in effective temperature

Effective temperature  $T_{\text{eff}}$  is usually used as the independent variable of a gyrochronology since it is set by radiated energy per unit area and is thus related to the eddy velocity and magnetodynamo strength in the convective envelope of a star. Precise and accurate determination of  $T_{\text{eff}}$  is a classic problem in stellar astrophysics, and a particularly acute issue for the coolest stars. Recent calibrations of the temperature scale of M dwarfs based on interferometric measurement of stellar radii, (*Gaia*) parallaxes, and the Stefan-Boltzmann law ([Boyajian et al. 2012](#); [Mann et al. 2015](#)) permit precision as good as 50 K, but most host stars have  $T_{\text{eff}}$  with precision no better than 75 K. The M67 gyrochrone of [Dungee et al. \(2022\)](#) was fit to the  $g-i$  colors of stars, and converted to  $T_{\text{eff}}$  using the temperature scale of [Mann et al. \(2015\)](#). This combined with the slope of the M67 gyrochrone will produce formal uncertainties

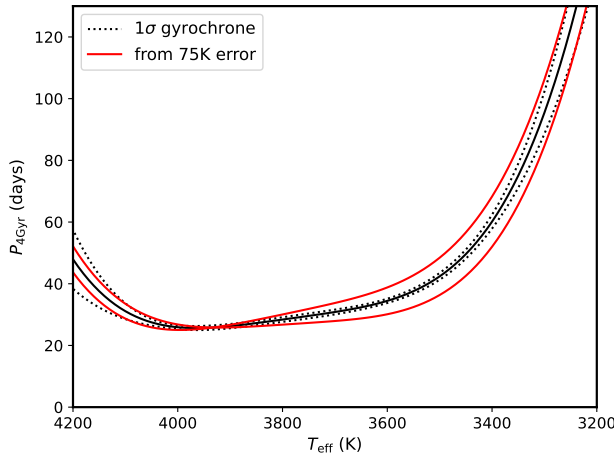


**Figure 3.** Intrinsic dispersion in the 4 Gyr-old M67 gyrochronone (dashed black lines) established by [Dungee et al. \(2022\)](#) and dispersion produced by errors in  $T_{\text{eff}}$  of 75K (red lines).

of 0–17% in age, with the largest value at the cool (3200K) end, decreasing to zero near 3900K, and rising to 12% at 4200K.

#### 5.4 Initial Rotation

A major contributor to age error is departure of a star’s behavior from a rotation-age relation due to variation in initial conditions, i.e angular momentum/rotation rate at an early age. A star that is initially spinning slower/faster than the mean of the population used to construct the gyrochronology will have an estimated age that is erroneously older/younger. Surveys of star-forming regions and very young clusters show that low-mass members emerge from their disk-hosting phase with a wide range of rotation rates at a given mass ([Cody & Hillenbrand 2010](#); [Rebull et al. 2016](#); [Venuti et al. 2017](#); [Rebull et al. 2018](#); [Kounkel et al. 2019](#); [Serna et al. 2021](#)), perhaps due to variations of disk lifetime brought on by differences in the tidal and ultraviolet environment of stars ([Kraus et al. 2012](#); [Roquette et al. 2021](#)). Since it is not possible to know the initial rotation of an individual star, this variation can induce significant uncertainty in derived ages. [Epstein & Pinsonneault \(2014\)](#) used rotational evolution models to show that this greatly limited the utility of rotation-based ages among cooler, older dwarfs.

The scatter in initial rotation rates can be estimated from observations of the PMS members of very young clusters. If AM loss through winds is small over the PMS interval, the fractional dispersion in rotation rate at a given mass should be conserved even as the stars contract and spin up. The fractional dispersion is also conserved during the saturated phase of magnetic activity because the torque is proportional to rotation rate and the spin-down is exponential with a rate-independent time constant. In the 130 Myr-old Pleiades, no well-defined rotational sequence exists for our range of  $T_{\text{eff}}$ /colors but there is a strong trend of decreasing  $P_{\text{rot}}$  (6–0.6 days) with decreasing  $T_{\text{eff}}$  ([Rebull et al. 2016](#)). An iterative fit to this over the equivalent de-reddened  $V - K$  color range (3.22–5.29) yields a *fractional* dispersion of 45% (see also Fig. 18 in [Stauffer et al. \(2016\)](#)), but this value does not reflect the numerous outliers, some of which may be binaries. Likewise, the rotation periods of members of the ∼150 Myr-old cluster NGC 2516 ([Fritzewski et al.](#)

[2020](#)) within this same color range have a scatter of  $\gtrsim 50\%$ , about one order of magnitude larger than what is observed at later epochs.

This large scatter in initial (ZAMS) rotation rates  $P_0$  will be compressed once the stars decelerate to the unsaturated regime at  $P_{\text{crit}} \sim 0.13\tau_c$  ([Wright et al. 2018](#)) where the torque becomes highly rotation rate-dependent and period-time trajectories flatten. In the saturated regime,  $P(t) = P_0 e^{t/T}$ , where  $T$  is the spin-down timescale ([Matt et al. 2015](#)), thus a star with a ZAMS rotation period that differs by  $\Delta P_0 \ll P_0$ , will reach  $P_{\text{crit}}$  at a time that differs by

$$\Delta t = -T \log \left( \frac{P_0 + \Delta P_0}{P_0} \right). \quad (3)$$

Because subsequent rotational evolution proceeds from the condition  $P = P_{\text{crit}}$ , independent of  $P_0$ , the star will experience the same rotation history, but delayed by  $\Delta t$ . Thus this is the error in gyrochronological age induced by  $\Delta P_0$ .  $T$  depends on the braking torque parameter and moment of inertia of the star. [Somers et al. \(2017\)](#) found that stars in mass bins of  $0.25 - 0.40M_{\odot}$  and  $0.40 - 0.60M_{\odot}$  lose 25% and 39%, respectively, of their AM in the  $\approx 115$  Myr interval between the age of the Upper Scorpius star-forming region and the Pleiades cluster, implying a spin-down timescale of 225–400 Myr. [Somers et al. \(2017\)](#) also found a dispersion of 0.21 and 0.44 dex in the specific (mass-normalized) AM of Pleiades stars for stars in these respective mass bins. Application of Eqn. 3 produces an age error of about 200 Myr, which for a nominal 4 Gyr-old star is 5%.

Finally, the intrinsic dispersion in the rotation sequences of cluster stars can be used to empirically estimate age error due to rotation rate dispersion. For stars undergoing power-law spin-down ( $P_{\text{rot}} \propto t^{\chi}$ , [Skumanich 1972](#)), the dispersion in age consistent with a given  $P_{\text{rot}}$  is related to the dispersion in period for a given age (i.e., in the co-eval population of a cluster):

$$\frac{\Delta t}{t} = \frac{1}{\chi} \frac{\Delta P}{P} \quad (4)$$

We measured the outlier-excluded dispersion  $\Delta P$  around the best-fit rotational sequence of M67 to be 1.6 days, but this is consistent with the 10% measurement errors alone, and the intrinsic dispersion could be smaller. The dispersion in other, younger ( $\lesssim 1$  Gyr) clusters like those observed by *K2* can be better determined, but with the caveat that Skumanich-like spin-down only applies to times much later than the era of saturated magnetic activity. A well-defined rotational sequence is apparent in the Praesepe cluster (upper right-hand panel of Fig. 4), estimated to be 600 Myr-old ([Gossage et al. 2018](#)). We fit a second-order polynomial with iterative  $3\sigma$  outlier rejection to 3500–4200K members with rotation periods cataloged by [Douglas et al. \(2019\)](#). (Cooler stars have yet to converge to an identifiable sequence.) The scatter is 0.97 days ( $N=121$ ). The same analysis applied to the much sparser Hyades sample yields the same dispersion: 0.95 days ( $N=13$ ), a fractional dispersion of about 5% (bottom left panel of Fig. 4). The data on M dwarfs in other, older clusters are much sparser: [Curtis et al. \(2019a\)](#) estimated a dispersion of  $\pm 10\%$  for the coolest stars in NGC 6819 ( $\approx 2.5$  Gyr) and Ruprecht 147 ( $\approx 2.7$  Gyr) but of these, only *five* stars have  $Gaia B_P - R_P$  colors that correspond to our  $T_{\text{eff}}$  range. Using the [Godoy-Rivera et al. \(2021\)](#) catalog of members of M37 ( $\approx 470$  Myr) [Frakou et al. \(2022\)](#) and NGC 6811 ( $\approx 950$  Myr) with rotation periods we estimate dispersions of 0.8 days ( $n=20$ ) and 0.6 days ( $n=12$ ) respectively (upper left and bottom right panels of Fig. 4). The existence of a rotation sequence among M37 M dwarfs is not clear. Some of the observed dispersion in these clusters is probably the result of errors in  $T_{\text{eff}}$ : for a standard error of 75 K, this is  $\sim 0.5 - 1$  day.

day, depending on cluster and  $T_{\text{eff}}$  (purple dotted lines in Fig. 4). Thus the actual period dispersion could be substantially lower than the observed values.

We adopted a conservative fractional dispersion in  $P_0$  of 5%, with the caveat that current data on the establishment of a rotational sequence at these epochs only extends to a spectral type of M2 ( $T_{\text{eff}} \sim 3550$  K). For  $n = 0.62$ , this corresponds to an age dispersion of 8% (Eqn. 4), which we incorporate in our MC realizations of age estimates by adopting a Gaussian distribution. These calculations assume that a rotational sequence has developed by the epoch of interest for the relevant  $T_{\text{eff}}$ , i.e., that stars have spun down into the unsaturated regime. This is not the outcome for M dwarfs in the models of Epstein & Pinsonneault (2014), which explains their large predicted age errors, but it is the case at least by 4 Gyr for this  $T_{\text{eff}}$  range (see Sec. 7.2).

#### 5.4.1 Metallicity

The rotational evolution of cool dwarf stars is expected to be metallicity-dependent through the effects of opacity and mean atomic weight on the interior structure and dynamics of the star, which in turn govern the moment of inertia, and the scale of convection that drives the dynamo responsible for star's magnetic field, activity, and mass loss through a wind. Moreover, at a fixed  $T_{\text{eff}}$ , a more metal-rich MS star will have a higher mass. The [Fe/H] of the nearby stellar clusters used to construct gyrochronologies is close to solar: M67, Ruprecht 147, and NGC 6811 are within uncertainties of solar (Pasquini et al. 2008; Bragaglia et al. 2018; Molenda-Żakowicz et al. 2014), while both Praesepe and the Hyades have  $[\text{Fe}/\text{H}] = +0.15$  (Cummings et al. 2017). However, stars in the solar neighborhood have metallicities ranging from  $-1$  to  $+0.5$  (Toyouchi & Chiba 2018), and the M dwarf stars observed by *Kepler* have a  $[\text{Fe}/\text{H}]$  distribution that is approximately Gaussian with a mean of  $-0.09$  dex and standard deviation of  $\pm 0.22$  dex (Gaidos et al. 2016).

We predict the effect of non-solar metallicity on the duration of the stellar PMS phase and the subsequent spin-down on the MS, which we model as exponential "saturated" spin-down from an initial rotation period  $P_0$  to the critical value  $P_{\text{crit}} = 0.13\tau_c$  at which the Rossby number exceeds a critical value 0.13 (Wright et al. 2018), and unsaturated, Skumanich-like power-law spin-down thereafter. The error in an age based on solar-metallicity gyrochrones induced by a non-solar metallicity is the sum of the variation in these two intervals. We used the Dartmouth standard (non-magnetic) models to compute these for a range of masses and [Fe/H] in 0.1 dex intervals from  $-0.7$  to  $+0.5$ . The MS saturated spin-down interval is taken to be:

$$T_{\text{sat}} = \frac{I}{n} \log \frac{P_{\text{crit}}}{P_0}, \quad (5)$$

where  $I$  is the moment of inertia (nearly constant for MS M dwarfs) and  $\Gamma$  is the (constant) torque parameter. Both  $I$  and  $P_{\text{crit}}$  are metallicity-dependent and were calculated using the Dartmouth models. We adopted the scaling relationship for the torque parameter from van Saders & Pinsonneault (2013), which is based on Matt et al. (2012):

$$\Gamma \propto R_*^{3.1} L_*^{0.56} M_*^{-0.22} p_{\text{phot}}^{0.44} \quad (6)$$

where  $p_{\text{phot}}$  is the pressure at the photosphere.  $p_{\text{phot}}$  will be proportional to gravity and inversely proportional to the specific opacity  $\kappa$ . The mass inferred for a given MS  $T_{\text{eff}}$  will also vary with [Fe/H] because the radius and hence luminosity changes. Using the  $M_* - M_{K_s}$  (mass-luminosity) relations of Mann et al. (2019), and exploiting the

fact that the bolometric correction for the  $K_s$ -band is only weakly dependent on [Fe/H] (Mann et al. 2015) and thus will be approximately fixed at a given  $T_{\text{eff}}$ ,  $L_* \approx M_*^{2.7}$  in this range. With that relation and the Stefan-Boltzmann law, at a given mass and  $T_{\text{eff}}$ , Eqn. 6 becomes:

$$\Gamma \propto R_*^{4.53} \kappa^{-0.44} \quad (7)$$

In the interiors of cool stars where bound-free opacity dominates, the opacity will scale linearly with the metal abundance  $Z \propto 10^{[\text{Fe}/\text{H}]}$ . We calculated for  $\Gamma$  for the solar-metallicity case by finding the age at which Skumanich-like rotational evolution marched backward from the M67 gyrochronne (Dungee et al. 2022) gives  $P_{\text{rot}} = P_{\text{crit}}$  and then setting  $\Gamma$  so that exponential spin-down from  $P_{\text{rot}} = P_0$  also reach  $P_{\text{crit}}$  at this age, i.e:

$$\Gamma = \frac{I_0}{4\text{Gyr}} \left( \frac{P_4}{P_{\text{crit}}} \right)^{1/0.62} \log \frac{P_{\text{crit}}}{P_0} \quad (8)$$

The PMS interval of M dwarfs is not readily defined since these stars gradually approach the MS. Since we are concerned only with the effect of stellar contraction on spin-up, we define the interval at which the timescale for contraction and spin-up (taken to be the logarithmic change in the momentum of inertia with time) greatly exceeds the timescale for spin-down by saturated magnetic activity. Here, we adopted "greatly" to be  $10\times$  but our estimates are not sensitive to the exact figure.

The top panel of Fig. 5 plots the variation in PMS duration relative to the solar-metallicity cases vs. [Fe/H] for the same mass/ $T_{\text{eff}}$  cases as the top panel. The middle panel of Fig. 5 plots variation of MS  $T_{\text{sat}}$  relative to the solar-metallicity value vs. [Fe/H] for 40 different mass tracks with MS  $T_{\text{eff}}$  falling within 3200-4200K. As one metric of the age error due to non-solar [Fe/H] we added the PMS and saturated spin-down durations and performed linear regression with [Fe/H] over the range of  $-0.3$  to  $+0.3$ , where most M dwarfs fall. This slope of this regression vs.  $T_{\text{eff}}$  is the light-colored curve in the bottom panel of Fig. 5. The sensitivity of the age estimates to [Fe/H] increases from 0.05 Gyr/dex at 3200K, peaking at 0.2 Gyr/dex at around 3900K, and declining in the K dwarf regime (Fig. 5). This behavior is almost entirely a consequence of the metallicity dependence of the braking torque (van Saders & Pinsonneault 2013), with a lesser contribution from changes in mass with metallicity at a fixed  $T_{\text{eff}}$ .

Although the power-law index of the Skumanich-like spin down observed on long time-scales is not considered metallicity-dependent, metallicity-dependent torque could still impart additional deviation from predictions based on solar-metallicity gyrochrones during the transition to purely power-law behavior. To quantify this, we performed calculations of rotation evolution using the models of Clayton et al. (2020b), which use the torque scaling of Eqn. 6. We used the stellar model interpolation and Markov Chain Monte Carlo (MCMC) tools in *kiauhoku* (Clayton et al. 2020a) to make  $P_{\text{rot}}$ -based age estimates of 4 Gyr-old model stars with a given  $T_{\text{eff}}$  and varying [Fe/H], but assuming solar [Fe/H]. We performed a linear regression of the inferred age minus the "true" age (4 Gyr) versus [Fe/H] for different values of  $T_{\text{eff}}$ , and the slope is plotted as the black curve in the bottom panel of Fig. 5. (These calculations do not go below 3500 K because of incompleteness in the model grid.) This curve has the same overall shape as our curve of PMS+MS age sensitivity (light colored curve) but is generally larger in magnitude, as expected.

Based on a comparison of the curves in Fig. 5a, we approximately incorporate the metallicity dependence of spin-down during the transition to pure Skumanich-like behavior by doubling the off-

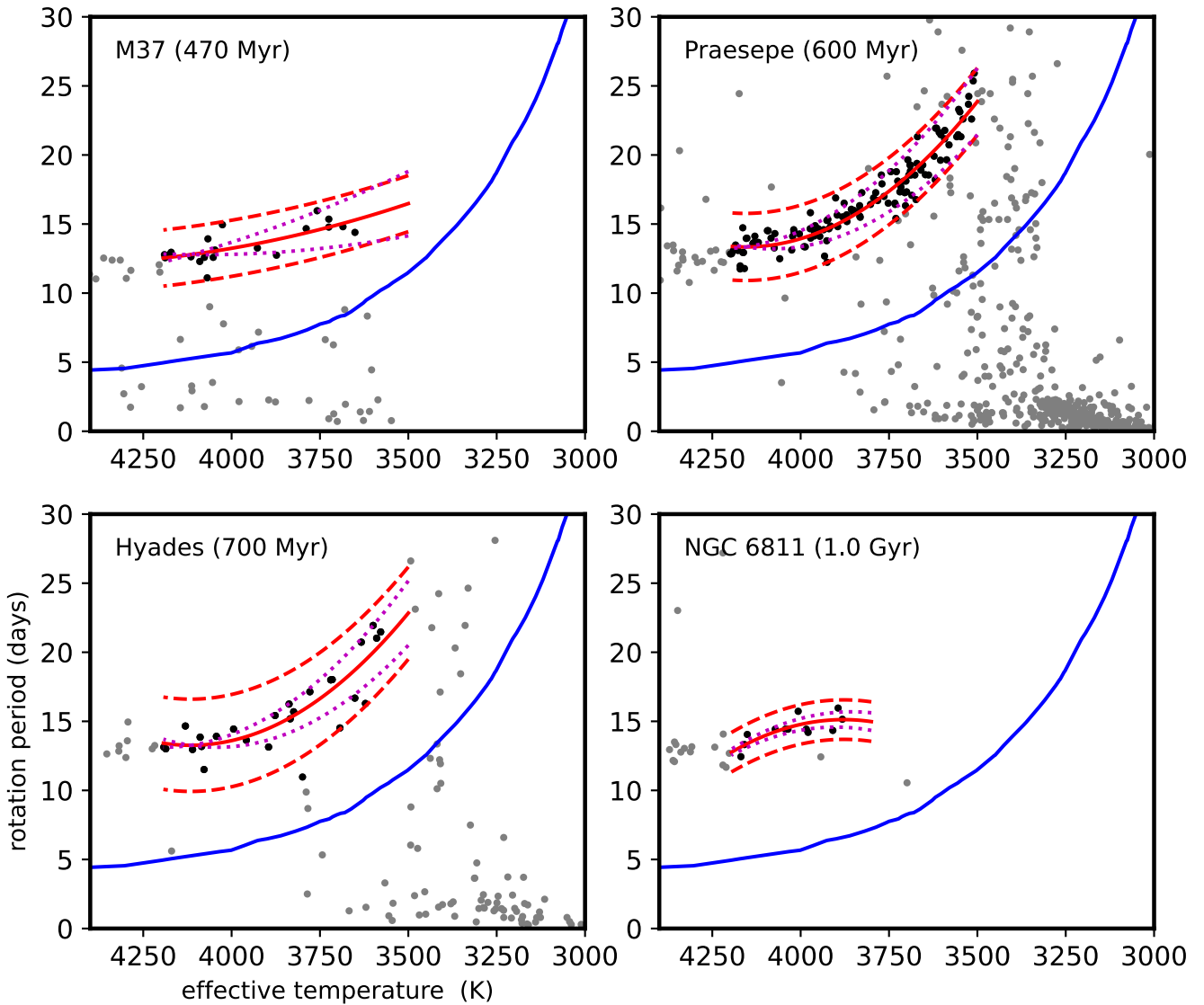


**Figure 4.** Fits of the cool dwarf rotational sequences of four open clusters. (The existence of a rotation sequence in M37 M dwarfs is unclear). Black points indicate stars used in iterative, outlier-rejection fits. The solid red line is the fit, the dashed red lines are the  $\pm 2.5\sigma$  rejection boundaries, and the dotted magenta lines show the extent of the scatter induced solely by an error of  $T_{\text{eff}}$  of 75K. The blue line is the critical rotation period for  $Ro = 0.13$  using the relation between convective turnover time and luminosity of Jeffries et al. (2011), with luminosities from the Dartmouth stellar evolution models (Dotter et al. 2008; Feiden 2016). Stars below this line will have saturated magnetic fields and experience exponential spin-down.

set during the MS saturated and adding it to the PMS offset. This is the heavy colored curve in the bottom panel. We multiply the slope by a typical uncertainty of  $\pm 0.1$  dex in [Fe/H] and add this (up to  $\pm 150$  Myr) to our error budget. We also use *kiauhoku* to calculate individual [Fe/H]-dependent *corrections* for the age of each star with known metallicity and  $T_{\text{eff}} > 3500$  K that can be added to age estimated from our solar-metallicity gyrochronology.

## 6 RESULTS: PLANET HOST STAR AGES

Table 6 provides the  $T_{\text{eff}}$  and [Fe/H] (if available) that were used for the gyrochronne calculations, the rotation period, the method and instruments used to obtain it and the reference, and the estimated age and uncertainty. If a metallicity is available, we also

provide, but do not incorporate, a *kiauhoku*-calculated value for the [Fe/H]-dependent correction. Only the first 50 entries are shown; the complete machine-readable table is provided on Zenodo (DOI: 10.5281/zenodo.7578269). Figure 6 compares the empirical ages of host stars to ages using generated with the *kiauhoku* model (Claytor et al. 2020a). There is good agreement among the warmer stars in the sample, but a clear trend of older *kiauhoku*-based estimates for cooler  $T_{\text{eff}}$ , where the models have not been calibrated. The systematic offset of model-derived ages for the coolest stars further illustrates the need for calibrators across the full range of temperature and age.

The distribution of ages assigned to Monte Carlo realizations is plotted in Fig. 7, where we have plotted the KOIs and all other host stars with separate curves as distinct in terms of sensitivity

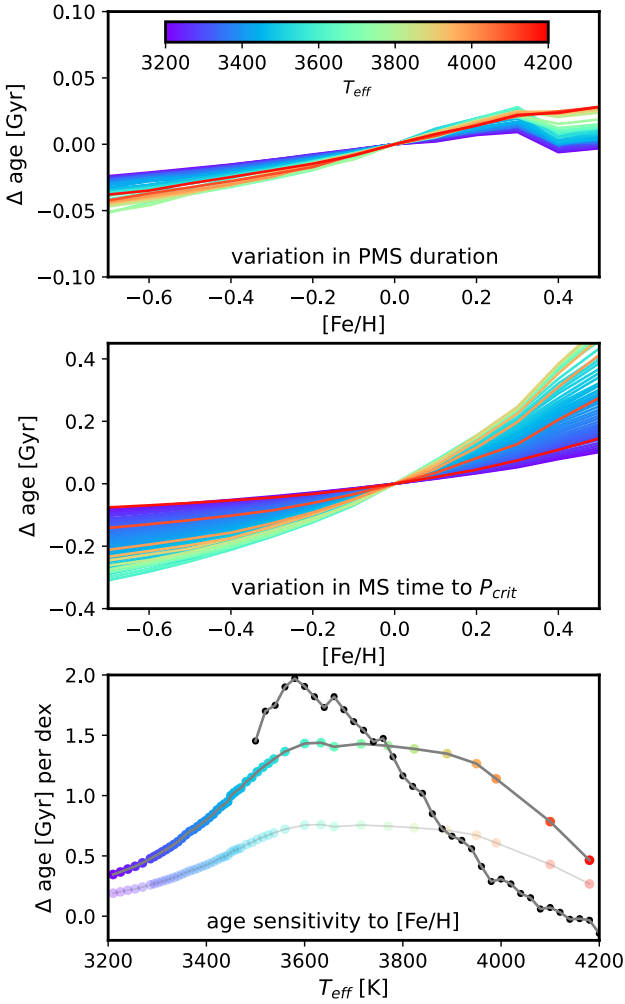


**Figure 5.** Difference in actual age relative to gyrochronic age due to non-solar metallicity due to variation in the PMS duration (a) and MS interval required for spin-down sufficiently for  $Ro$  to exceed the critical value 0.13 and the star to leave the saturated phase of activity and follow power-law Skumanich-like spin-down (middle). Positive values means that a star will be older than its gyrochronologic age. Each color corresponds to a different mass track in Dartmouth standard model calculations, converted to  $T_{\text{eff}}$  on the main-sequence using the empirical relation of [Pecaut & Mamajek \(2013\)](#). The light colored line in the bottom panel is the slope of the summed intervals vs.  $[\text{Fe}/\text{H}]$  obtained at each value of  $T_{\text{eff}}$ . The black curve is the slope calculated from a full model of metallicity-dependent spin-down over a representative age of 4 Gyr. The heavy colored line is the PMS interval plus twice the MS interval used as an approximation for the actual sensitivity that reproduces the shape and magnitude of the model simulations.

and systematics as well as (potentially) stellar populations, and compare these to the isochrone-based distribution for all *Kepler* stars from [Berger et al. \(2020\)](#). For upper limits, ages were drawn from a uniform distribution from zero to the upper limit. We did not exclude known binary stars from these distributions since the effect of binaries depends on semi-major axis in a manner that is still being actively investigated (e.g., [Messina 2019](#)).

To help discern between actual structure and systematics in the age distribution, we created a mock stellar population with a uniform age distribution,  $T_{\text{eff}}$  drawn with replacement from the actual catalog, and  $P_{\text{rot}}$  calculated with a simple model of the spin-

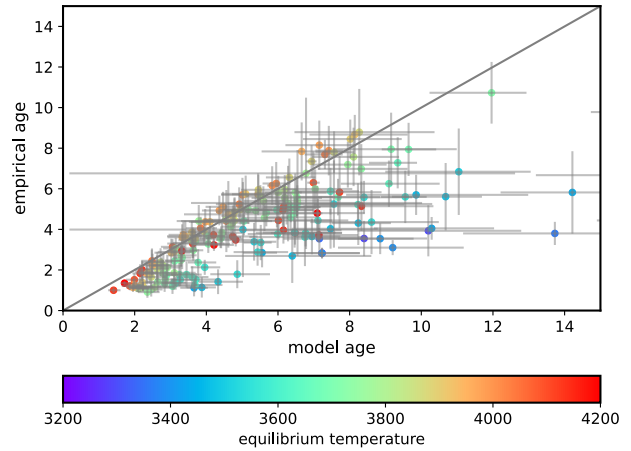


**Figure 6.** Empirical ages of host stars based on the rotation-age relations in Fig. 2 vs. the estimates using the *kiauhoku* model ([Clayton et al. 2020a](#)).

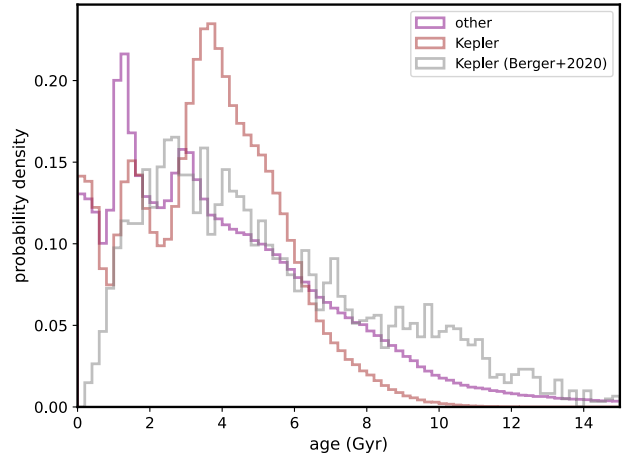


**Figure 7.** Distribution of estimated ages for KOIs and all other known M dwarf host stars, accounting for the uncertainties. The grey curve is the isochrone-based age distribution for all *Kepler* stars from [Berger et al. \(2020\)](#).

down of stellar population. The model assumed solid-body rotation and power-law spin-down with index  $\gamma = 0.62$  for  $Ro > 0.13$ , i.e., at MS ages  $t > t_{\text{crit}}$  where the condition  $P_{\text{rot}} > P_{\text{crit}}$ , as defined before, is satisfied. For main-sequence ages  $t < t_{\text{crit}}$ , stars undergo exponential spin-down with a time constant set such that at  $t = 0$ ,  $P_{\text{rot}}$  is equal to an initial value  $P_0$ . The initial period is derived from the specific momentum distribution of among  $\sim 10$  Myr-old M dwarf members of the Upper Scorpius star-forming region ([Somers et al. 2017](#)), and the moments of rotational inertia from the Dartmouth stellar evolution models. Main sequence ages were a random draw from a uniform 0–10 Gyr distribution, minus the PMS duration as taken from Dartmouth solar-metallicity models ([Dotter et al. 2008](#)). (The  $P_{\text{rot}}$  of PMS stars is fixed at  $P_0$ , but this choice is not important since these stars were subsequently excluded.) We added the Gaussian-distributed error of 7.4% to the periods, the median of the distribution of actual error, and then derived the ages and

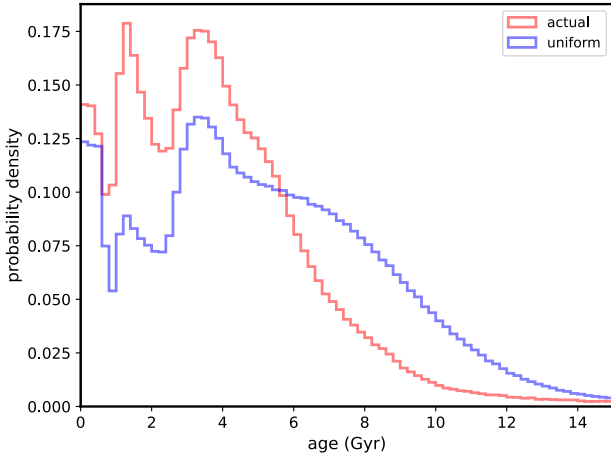


**Figure 8.** Distribution of actual ages vs. those inferred from a “mock” population of stars with the same  $T_{\text{eff}}$  distribution as the exoplanet host stars, but a uniform 0–10 Gyr age distribution (see text for details).

errors with the same routines used for the actual exoplanet host star catalog. The actual and mock distributions are compared in Fig. 8.

There is a marked deficit and marked structure at  $<3$  Gyr in the age distribution of stars in both the *Kepler* and non-*Kepler* samples (Fig. 7), but this feature also appears in the simulation of a uniform distribution of age (Fig. 8), showing that the inferred age distribution is heavily affected by systematics, i.e. the incomplete working gyrochronology over the entire  $T_{\text{eff}}$  range at young ages. Monte Carlo realizations that fall in these gaps are assigned upper limits and thus not correctly represented in this distribution. Both the inferred *Kepler* and non-*Kepler* distributions decline with age, and more rapidly than that inferred from the mock uniform-age population. A declining rotation-based age distribution was also inferred for solar-type *Kepler* host stars and is in part a bias caused by the difficulty of detecting the lower amplitude, longer period rotational signals that are more prevalent around older stars (Walkowicz & Basri 2013). This pattern is also mimicked by an age distribution of *Kepler* target stars based on isochrone analysis (Berger et al. 2020, grey curve in Fig. 7); this is also biased towards younger (and more massive stars) that evolve more quickly. The *Kepler* distribution peaks at older ages than the non-*Kepler* sample, which could be due to the greater sensitivity and longer monitoring interval of the prime mission, but perhaps also because *Kepler* was observing a field centered at  $b = 13$  deg containing a slightly older population further above the Galactic plane. The *Kepler* distribution terminates at 10 Gyr, about the age of the Galactic disk. The distribution of non-*Kepler* host stars has a tail that extends well beyond 10 Gyr but this is largely due to host stars with significant uncertainties in  $P_{\text{rot}}$ , along with a handful of binaries (see below).

**Binaries:** Twenty-six of the 249 planet host stars are known to have stellar companions. This 11% fraction is much lower than  $26.8 \pm 1.4\%$  among field M dwarfs (Winters et al. 2019). Since exoplanet hosts are comparatively well-studied among cool field stars, this is very unlikely due to limited characterization of these stars. Instead, it probably reflects survey/detection bias where binary stars are avoided in exoplanet surveys because it is usually more difficult to detect planets around them (Kraus et al. 2016; Ziegler et al. 2018, 2021; Su et al. 2021; Clark et al. 2022), and because contamina-

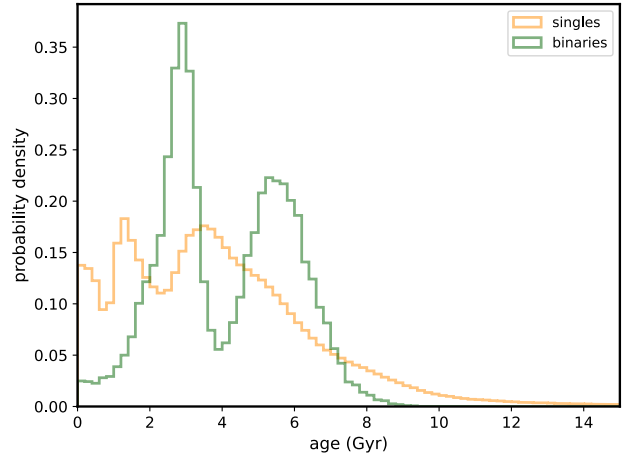


**Figure 9.** Distribution of estimated ages for single vs. binary/multiple host stars, accounting for the uncertainties. The irregularity of the binary distribution is sampling noise: only 26 systems constitute the binary sample.

tion of the host star signal by other stars is detrimental to precise measurement of RVs (Cunha et al. 2013).

The rotational history of stars in multiple systems can differ greatly from that of single stars. Stars with stellar companions are more likely to be rapidly rotating relative to single stars of the same age/mass (Kraus et al. 2012; Simonian et al. 2019). Very close ( $\ll 1$  au) binaries transfer orbital AM to rotational AM via tidal torques (Fleming et al. 2019). At moderate separations ( $\sim 100$  au) a stellar companion will truncate a disk and shorten its viscous lifetime (Cieza et al. 2009; Kraus et al. 2012; Rosotti & Clarke 2018). This removes a sink of stellar angular momentum, allowing the star to spin-up unimpeded during pre-main sequence contraction (Messina 2019).

We computed ages based on rotation without regard to multiplicity, but warn that in the case of binaries, such ages could be seriously in error. In this sample, at least, the distribution of rotation periods does not appear remarkably different from single stars (Fig. 1) nor does the age distribution of known binaries appear remarkable (Fig. 9), although it is greatly limited by the small sample size. This could be because the smaller fraction of binaries that do appear in the catalog tend to be very wide, and the effects on rotation and hence age are negligible.

**Anomalously old stars:** Four host stars (GJ 27.1, GJ 667 C, HD 238090, and HIP 70849) are assigned problematic ages that are  $> 2\sigma$  older than 10 Gyr, the nominal age of the Galactic disk. These are unlikely to be Galactic halo or former globular cluster members because unusual abundances and peculiar motion characteristic of such stars would have been noted. Three of the stars are in binaries, in which stellar companions could directly or indirectly affect the rotation evolution. The fourth, GJ 27.1, has a  $140 \pm 10$  day rotation period estimated from ASAS-SN photometry, far longer than that expected for an early-type M dwarf in the Galactic disk, and the age is obviously unphysical:  $35 \pm 9$  Gyr. The star’s metallicity has not been reported. Potentially the rotation period is an artifact, e.g., confusion with another star (the survey’s resolution is 15”).

**Young stars:** No PMS-ages were assigned to our stars, which is expected since we removed all known disk-hosting and PMS stars from our catalog. Fourteen stars can only be assigned upper limits for ages, and of these 8 are younger than 1 Gyr at the 95-percentile

**Table 1.** TIME-Table: Catalog of Cool Host Stars with Established Rotation Periods.<sup>1</sup>

Name	$T_{\text{eff}}$ [K]	Fe/H [dex]	Period (unc) [days]	Method <sup>2</sup> (Instruments <sup>3</sup> )	Reference	Age (unc) Gyr	Corr <sup>4</sup> Gyr	Note <sup>5</sup>
EPIC 201170410	3650	-0.05	20.16 (1.6)	P (K2)	this work	1.77 (0.58)	+0.00	
EPIC 211822797	3856	+0.14	15.88 (0.72)	P (K2)	Reinhold & Hekker (2020)	1.18 (0.24)	+0.03	
G 264-012	3326	+0.10	100.0 (6.0)	PS (TE/ME/AN/CA)	Amado et al. (2021)	6.66 (3.26)	+0.12	
G 9-40	3713	+0.04	34.08 (11.46)	P (K2)	Reinhold & Hekker (2020)	5.35 (2.57)	+0.00	
GJ 1132	3270	-0.12	122.3 (5.5)	P (ME)	Cloutier et al. (2017)	6.31 (3.23)	—	
GJ 1148	3304	+0.16	73.5	P (HA)	Hartman et al. (2011)	4.44 (1.6)	+0.51	no error
GJ 1214	3252	+0.29	125.0 (5.0)	P (ST)	Mallonn et al. (2018)	5.91 (3.0)	—	
GJ 1252	3458	+0.10	64.0 (4.0)	P (WA)	Shporer et al. (2020)	6.61 (2.34)	+0.58	
GJ 1265	4052	-0.04	29.17 (6.27)	P (K2)	Reinhold & Hekker (2020)	4.44 (1.53)	+0.11	
GJ 15 A	3607	-0.32	43.82 (0.56)	PS (Fa/HI)	Howard et al. (2014)	5.87 (1.14)	-0.66	binary
GJ 176	3680	+0.14	38.92	P (AS)	Kiraga & Stepień (2007)	5.6 (0.9)	+0.52	no error
GJ 229	3790	—	27.3	P (AS)	Suárez Mascareño et al. (2016)	3.77 (0.51)	—	binary,no error
GJ 251	3389	-0.03	122.1 (2.05)	PS (WA/CA)	Stock et al. (2020)	12.52 (5.86)	—	
GJ 27.1	3578	—	139.0 (3.5)	P (AS)	this work	34.94 (7.93)	—	too old
GJ 273	3317	+0.09	93.5 (16.0)	S (HA)	Suárez Mascareño et al. (2017)	6.12 (3.17)	+0.09	
GJ 3138	3899	-0.30	42.5	S (HA)	Astudillo-Defru et al. (2017a)	8.44 (0.95)	+0.14	no error
GJ 3293	3600	+0.11	41.0	S (HA)	Astudillo-Defru et al. (2017a)	5.19 (1.06)	+0.40	no error
GJ 338 B	3770	-0.03	10.17	P (K2)	Magaudda et al. (2020)	<0.91	—	binary,no error
GJ 3470	3611	+0.20	20.7 (0.15)	P (Fa)	Biddle et al. (2014)	1.65 (0.54)	+0.16	
GJ 3473	3347	+0.11	168.3 (3.65)	P (ME/TJ)	Kemmer et al. (2020)	16.46 (8.46)	—	binary
GJ 357	3480	-0.12	77.8 (2.1)	P (AS/AN/NS)	Luque et al. (2019)	9.76 (3.31)	-0.30	
GJ 367	3687	-0.01	48.0 (2.0)	P (WA)	Lam et al. (2021)	7.95 (1.31)	+0.04	
GJ 3779	3324	+0.00	95.0 (5.0)	PS (ME/CA)	Luque et al. (2018)	6.13 (2.87)	—	
GJ 3929	3369	+0.00	122.0 (13.0)	P (HA/AN)	Kemmer et al. (2022)	11.1 (5.76)	-0.36	
GJ 393	3548	-0.18	34.15 (0.22)	P (K2)	Amado et al. (2021)	3.32 (0.87)	-0.24	
GJ 3942	3850	-0.04	16.3 (0.1)	PS (AS/HA)	Suárez Mascareño et al. (2018)	1.18 (0.24)	+0.01	
GJ 3998	3825	-0.16	33.0	P (AP)	Giacobbe et al. (2020)	5.25 (0.69)	—	no error
GJ 411	3719	-0.36	56.16 (0.27)	P (Fa)	Díaz et al. (2019)	10.73 (1.52)	-0.52	
GJ 414 A	4120	+0.24	40.0 (4.0)	P (KE)	Dedrick et al. (2021)	5.87 (1.77)	+0.51	binary
GJ 4276	3440	+0.12	6.14	P (AP)	Giacobbe et al. (2020)	—	—	no age,no error
GJ 436	3479	+0.01	44.1 (0.2)	P (Fa)	Lothringer et al. (2018)	4.32 (1.09)	+0.00	
GJ 486	3290	-0.15	49.9 (5.5)	P (AS/LC/WA/TJ/OS)	Caballero et al. (2022)	3.51 (0.81)	-0.13	
GJ 514	3755	-0.09	30.0 (0.9)	S (HA)	Suárez Mascareño et al. (2017)	4.11 (0.6)	+0.03	
GJ 581	3490	-0.09	130.0 (2.0)	S (HA)	Robertson et al. (2014)	23.26 (7.7)	—	
GJ 625	3540	-0.35	76.79 (0.13)	P (WA)	Díez Alonso et al. (2019)	11.96 (3.14)	—	
GJ 628	3305	-0.02	89.3 (1.8)	P (Fa)	Kane et al. (2017)	5.27 (2.32)	—	
GJ 649	3741	+0.03	23.8 (0.1)	P (AS)	Díez Alonso et al. (2019)	2.96 (0.51)	+0.11	
GJ 667 C	3755	—	103.9 (0.7)	S (HA)	Suárez Mascareño et al. (2015)	30.59 (4.06)	—	binary,too old
GJ 674	3453	-0.28	35.0 (0.1)	P (AS)	Suárez Mascareño et al. (2016)	2.85 (0.72)	-0.28	
GJ 676 A	3827	+0.23	41.2 (3.8)	S (HA)	Suárez Mascareño et al. (2015)	7.58 (1.46)	+0.56	binary
GJ 685	3844	+0.10	19.3 (0.3)	P (TJ)	Díez Alonso et al. (2019)	2.25 (0.36)	+0.15	
GJ 687	3439	+0.05	61.8 (1.0)	P (Fa)	Burt et al. (2014)	5.82 (1.99)	+0.42	
GJ 720 A	4013	+0.01	36.05 (1.41)	S (HA)	González-Álvarez et al. (2021)	6.26 (1.05)	+0.21	binary
GJ 740	3832	+0.08	35.56 (0.07)	S (CA/HA)	Toledo-Padrón et al. (2021)	5.97 (0.72)	+0.32	
GJ 832	3522	-0.30	45.7 (9.3)	S (HA)	Suárez Mascareño et al. (2015)	5.2 (2.13)	-0.98	
GJ 849	3551	+0.25	39.2 (6.3)	S (HA)	Suárez Mascareño et al. (2015)	4.33 (1.55)	+0.68	
GJ 876	3472	+0.17	31.31 (8.15)	P (K2)	Reinhold & Hekker (2020)	2.7 (1.35)	+0.29	
GJ 96	3892	+0.14	29.5 (0.5)	P (WA)	Díez Alonso et al. (2019)	4.67 (0.52)	+0.47	
GJ 9689	3880	-0.11	39.3 (0.4)	S (HA)	Maldonado et al. (2021)	7.35 (0.82)	+0.18	
Gl 49	3740	+0.13	18.4 (0.7)	S (HA)	Suárez Mascareño et al. (2018)	1.55 (0.41)	+0.07	binary

<sup>1</sup>The full table is available as a machine-readable table (DOI:10.5281/zenodo.7578269)<sup>2</sup>P = photometric. S = spectroscopic.<sup>3</sup>AN=All-Sky Automated Survey for Super-Novae (ASAS-SN, Kochanek et al. 2017), AP=APACHE (Sozzetti et al. 2013); AS=All Sky Automated Survey (ASAS, Pojmanski 2002); CA=CARMENES (Quirrenbach et al. 2016), ES=ESPRESSO (Pepe et al. 2021); FA=Fairborn (Henry 1999); HA=HARPS (Pepe et al. 2000); HN=Hungarian Automated Telescope Network (HAT-Net, Bakos et al. 2004); K2=K2 (Howell et al. 2014), KE=Kepler (Borucki et al. 2010); LC=Las Cumbres Observatory Global Telescope (LCO, Brown et al. 2013); ME=MEarth (Berta et al. 2012), NS=Northern Sky Variability Survey (NSVS, Woźniak et al. 2004); OS=Observatorio de Sierra Nevada; SP=SPIRou (Donati et al. 2020); ST=STELLA (Strassmeier et al. 2004); TE=TESS (Ricker et al. 2014); TJ=Telescope Joan Oró (TJO, Colomé et al. 2010); WA=Wide Angle Search for Planets (WASP, Pollacco et al. 2006).<sup>4</sup>Metallicity-dependent age correction to be added to value for solar-metallicity.<sup>5</sup>If no period error is provided, an uncertainty of 1 day is assumed.

level and not known to be binaries. The rotation period of one of these, TOI-620, is tentative and the star is also a suspected binary (Reefe et al. 2022). The other seven are *K2*-detected systems: K2-43, K2-239, K2-240, which hosts two transiting Neptune-size planets, has been detected in X-rays (Foster et al. 2022); K2-284, previously reported having a young age by David et al. (2018), K2-324, K2-354, and KOI-5879, a flaring M dwarf (Yang & Liu 2019).

### 6.1 Individual Noteworthy Systems

**GJ 229:** The nearby (5.76 pc) M1 dwarf Gliese/GJ 229 has an ultra-cool (T7-type) dwarf companion (Nakajima et al. 1995). The primary's 27.3-day rotation period was determined from ASAS-SN photometry (Suárez Mascareño et al. 2016) and we estimate an age of  $3.8 \pm 0.5$  Gyr, with the caveat that the existence of the companion on a 29 au orbit could have affected the rotation history. No uncertainty in  $P_{\text{rot}}$  was reported but this is likely to be small given the multi-year baseline of ASAS-SN.

**GJ 1214:** This nearby M4-type dwarf with a well-studied transiting “sub”-Neptune-size planet on a 1.58-day orbit (Charbonneau et al. 2009). Based on the  $125 \pm 5$  day rotation period identified in STELLA photometry by Mallonn et al. (2018), we estimate an age of  $5.9 \pm 3.1$  Gyr.

**LHS-1815:** This M1-type dwarf (aka TOI-704) hosts a transiting Earth-size planet on a 3.8-day orbit. The star lies 1.8 kpc above the Galactic plane and kinematically belongs to the “thick” Galactic disk population (Gan et al. 2020). We estimate an age of  $7.3 \pm 1.3$  Gyr, consistent with the expected age of that population.

**K2-22:** K2-22 is a late K dwarf that hosts what has been proposed to be a “evaporating” planet on a 9-hour orbit that manifests itself as quasi-periodic dimming due to accompanying dust cloud (Sanchis-Ojeda et al. 2015). The highest peak in a Lomb-Scargle periodogram in K2 photometry, is at  $7.61 \pm 0.26$  days but the shape of the lightcurve (Fig. A1) suggests this is one-half the period (Sanchis-Ojeda et al. 2015). A period of  $15.2 \pm 0.5$  days yields an estimated age of  $1.1 \pm 0.2$  Gyr, but this star has an M dwarf companion at a projected separation of 460 au Sanchis-Ojeda et al. (2015) which could have affected its rotation history.

**Barnard’s Star (GJ 699):** This very metal-poor, high peculiar motion M4-type is classified as intermediate between the Galactic Disk and Halo populations (Gizis 1997); a putative Doppler RV-detected planet (Ribas et al. 2018) around this star has been disputed (Lubin et al. 2021). It is *not* in our current catalog because its  $T_{\text{eff}}$  is marginally cooler than our 3200K cut-off, but, motivated by its unusual nature and recently confirmed  $P_{\text{rot}}$  of  $145 \pm 15$  days (Toledo-Padrón et al. 2019; Terrien et al. 2022), we compare this to the cool extremum of the Dungee et al. (2022) M67 gyrochron, which reaches 120 days at 3250K (Fig. 3) and at cooler temperatures is essentially an unconstrained extrapolation. Thus the gyrochronology suggests an age older than M67, as expected, but extension of M dwarf gyrochrones into the fully convective area is needed before assigning any robust age.

## 7 SUMMARY AND DISCUSSION

### 7.1 Rotation and Ages of M dwarf Exoplanet Hosts

The value of robust ages for exoplanet studies, and advances in the gyrochronology of older cool M dwarfs motivated us to catalog rotation periods among late K and early M-type dwarfs ( $T_{\text{eff}}=3200\text{--}4200\text{K}$ ) that host known planets, and to apply empirical,  $T_{\text{eff}}$ -

dependent rotation-age relations to estimate ages and their standard errors. This complements work on calibrated rotation-based ages among younger PMS stars (Kounkel et al. 2022). We cataloged 249 stars with rotation periods, 227 of which we are able to estimate ages with a median error of 20% and mode of 14%, and to an additional 8 we assign upper limits (Table 6). Our fractional error is significantly higher than the 5-10% estimated by Otani et al. (2022), probably because we include additional potential sources of error. Figure 10 shows ages of candidate or confirmed planets around these stars and the distribution with semi-major axis, radius, and equilibrium temperature, as reported in the NASA Exoplanet Archive.

The age distributions of both *Kepler* and non-*Kepler* host stars peak at around 3 Gyr with a steady decline to near zero at 10 Gyr, the age of the Galactic disk (Fig. 7). The resemblance of the actual and “mock” populations (the latter with a uniform 0-10 Gyr age distribution) shown in Figure 8 indicates that the structure of the distribution, particularly at young ages, is partly due to the discontinuous and limited coverage of the current gyrochronology and dispersion of the distribution due to error. The peaks at  $<3$  Gyr correspond approximately with the location of the calibration ages, and are likely artefacts due to ages that cannot be assigned in certain regions of  $T_{\text{eff}}\text{-}P_{\text{rot}}$  space and have only upper limits assigned. Other effects impacting the derived distribution include the opposing biases against detection of planets around younger, more rapidly rotating, and more active stars (Miyakawa et al. 2022), and against detection of rotational variability among older, slowly rotating, less active stars (Morris 2020).<sup>2</sup> Several versions of the local star formation history based on white dwarf cooling ages and *Gaia* astrometry also peak at around 3-5 Gyr (Isern 2019; Morris et al. 2019; Alzate et al. 2021), so the distribution of host star ages could reflect this. Our error analysis (Sec. 5) shows that one limiting source of error could prove to be the precision of stellar parameters, i.e.  $T_{\text{eff}}$  and [Fe/H]. The sensitivity to  $T_{\text{eff}}$  is due to the steepness of rotation sequences for very cool dwarfs.  $T_{\text{eff}}$ , which is related to the surface brightness and hence convective vigor of a star, is the appropriate independent variable for gyrochronology, but must be inferred from observables. The ultimate limit on accurate values of  $T_{\text{eff}}$  precision for M dwarfs is the challenge of establishing a reliable temperature scale.

### 7.2 Caveats and Limitations

We have adopted the values and standard errors of  $P_{\text{rot}}$  from the literature at face value. The possibility that the true period is twice the published value needs to be considered in cases of stars with anomalous rapid rotation and young ages. Ground-based observations can also suffer from aliasing imposed by diurnal, lunar, and annual window functions.

Our gyrochronology assumes that the narrow rotational sequence observed among the late K dwarfs and the warmer M dwarfs in the 2.7 Gyr-old Ruprecht 147 cluster (Curtis et al. 2020) extends to 3200K by 2.7 Gyr, and that the  $n = 0.62$  power-law spin-down derived by (Dungee et al. 2022) also applies to cooler M dwarfs at later times. This assumption could fail if the rotational sequence among M67 M dwarfs was formed by stalling, rather than a transition from saturated to un-saturated braking laws. Core-envelope re-coupling is expected to become weaker and take longer towards the fully convective boundary, which could mean that a rotational

<sup>2</sup> “Stalling” of spin-down due to core-envelope decoupling would result in broadening of the age distribution, not peak formation.

sequence appears much later, or not at all. This depends in part on the  $T_{\text{eff}}$  or mass dependence of the core-envelope coupling time vs.  $\tau_c$ . This issue can only be resolved by deeper monitoring of Ruprecht 147 or a cluster of similar age.

Another contributor to our error budget is sensitivity of the rotation-age relation to non-solar [Fe/H]. In the absence of appropriate calibration, we relied entirely on theoretical models to estimate this effect. The part due to changes in the structure and moment of inertia of the star is reasonably well-constrained by observations, but magnetic field pressure could modulate this. A model that includes this effect (Feiden 2016) predicts that at a fixed  $T_{\text{eff}}=3700\text{K}$ , inclusion of magnetic pressure increases the moment of inertia by 40%, but this is almost entirely due to a change in the mass inferred for a given  $T_{\text{eff}}$ . More uncertain is the metallicity-dependence of the torque, which, at least in our models, dominates the sensitivity. We based this scaling on the magnetized wind formulation of Matt et al. (2012) as reformulated by van Saders & Pinsonneault (2013), but this was developed for solar-type stars with rotationally-aligned dipole fields.

Finally, rotation-based ages for binary systems must be carefully considered, particularly given the possibility of a third, closer and unresolved component (Reipurth & Mikkola 2012). While most published exoplanets have had some sort of screening for binaries, not all of them cover all the parameter space, and surveys of very cool KOIs are only now coming to fruition.

### 7.3 Outlook

Since  $T_{\text{eff}}$  is not an observable and cannot be readily derived without stellar radii, gyrochrones could be established in a common reddening-corrected color which is also available for stars of interest; ideally, this color should be directly related to  $T_{\text{eff}}$ , it should be relatively [Fe/H]-independent. It should also use redder filters in which M dwarfs are comparatively bright and reddening is smaller. These requirements impact the use of *Gaia* photometry since M dwarfs are faint in the  $B_p$  synthetic band used to construct  $B_p - R_p$  colors. Analysis of color magnitude diagrams of *Kepler* M dwarfs using PanSTARRS photometry suggest that  $g-Y$  holds promise (A. Ali, pers. comm.).

Establishing precise M dwarf metallicities is a work in progress (e.g., Passegger et al. 2022). More challenging will be to validate the effect of metallicity on rotation-age relations, which here we have here treated only via stellar interior models and torque-law scaling. Tests of the metallicity-scaling of the torque law are desperately needed. Metal-poor or metal-rich clusters are relatively rare (Heiter et al. 2014) and thus, statistically, found at greater distances where observations to establish rotational sequences will be challenging. The wealth of binaries provided by *Gaia* (El-Badry et al. 2021) might serve as a road to calibration over a wider range of stellar parameters (Otani et al. 2022), provided sufficiently wide examples can be identified and precise ages for the primaries can be determined by other means.

Gyrochronology of exoplanet host stars is an ongoing effort and we envision the TIME-Table to be a “living” catalog of very cool dwarf rotation periods and ages that is periodically updated and revised with new discoveries and advances in gyrochronology. New planetary systems are constantly being detected, validated, or confirmed, particularly by the *TESS* mission, now in its fifth year. Rotational variability is being detected by two ongoing space surveys: *TESS* and, with much longer baseline but much sparser cadence, *Gaia* (Distefano et al. 2022). Ground-based surveys like ZTF and the Rubin Observatory (Hambleton et al. 2022) can provide

observations of distant field stars and young clusters. Although the *TESS* 27-day sector interval severely limits its ability to detect the rotation of older field stars (Claytor et al. 2022), those stars in and around the two Continuous Viewing Zones around the ecliptic poles are observed for multiple sectors and in principle it is possible to detect longer periods (Hedges et al. 2020; Claytor et al. 2022).

Many rotation periods have been established by analysis of Doppler RV residuals or indicators of activity in the time-series high-resolution spectroscopy obtained to detect, confirm, or measure the masses of planets (Suárez Mascareño et al. 2015). Terrien et al. (2022) showed that detection of the periodic signal in the Zeeman broadening of lines can reveal rotation of magnetic active regions on the star and yield a rotation period. The Zeeman effect increases with wavelength-squared, and the proliferation of high-resolution spectrographs operating in the infrared could lead to additional rotation periods using this approach. Alternatives to Lomb-Scargle periodogram analysis which are more robust to spot evolution such as autocorrelation and Gaussian process regression (Angus et al. 2018; Nicholson & Aigrain 2022) could be used to obtain more precise ages. Age-dating could also adopt a Bayesian approach, with Galactic population age distributions as priors (e.g., Mor et al. 2019; Cukanovaite et al. 2022).

Last but not least, additional observations of open clusters for calibration will improve the gyrochronology and lead to more precise (and hopefully more accurate) ages. In particular, the  $T_{\text{eff}}$  range of existing gyrochrones (including M67) should be extended through the fully convective boundary to include mid- and late-type M dwarfs representing hosts stars of particular interest (e.g., TRAPPIST-1), and, foremost, to establish whether a narrow rotational sequence appears by a few Gyr — without which gyrochronology is futile. The small effective area and large pixel size of *TESS* greatly limits its utility here, since older clusters are rare and hence more distant. The *Plato* mission will offer only limited improvement over *TESS* (15" vs. 20" pixels). However, the *Roman Space Telescope* will have a field of view of 0.28 deg<sup>2</sup> with 0.11" pixels. Ages of calibrator clusters could see refinement from a combination of *Gaia* parallaxes, asteroseismology, and high-throughput spectroscopy (Fu et al. 2022). Otherwise, much of the observations need to be performed from the ground using wide-field telescopes with sufficient aperture. Wide-field adaptive optics can alleviate the issues of source confusion in the fields of more distant clusters. For example, ground-layer adaptive optics (GLAO) can provide a factor of 2–3 improvement in spatial resolution compared to seeing-limited observations while still capturing an entire cluster in one observation (Rigaut 2002). Such improvements enable observations of dwarfs to spectral type M7 in the majority of clusters older than 1 Gyr (Dungee 2022)<sup>3</sup>.

### ACKNOWLEDGEMENTS

This work is dedicated to the memory of F.C.G., for whom the very stars of heaven were new. E.G. and R.D. were supported by NSF Astronomy & Astrophysics Research Program Grant 1817215. We thank Jen van Saders and an anonymous reviewer for helpful feedback on earlier versions of this manuscript. This paper includes data collected by the *Kepler* and *TESS* missions and obtained from the MAST data archive at the Space Telescope Science Institute

<sup>3</sup> <https://scholarspace.manoa.hawaii.edu/collections/67c8d51f-97a4-4d45-8a69-8baeaacaeaf6>

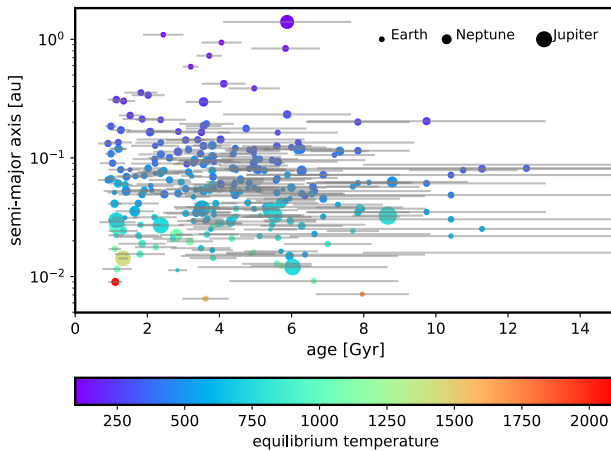


**Figure 10.** 111 confirmed planets with properties from the NASA Exoplanet Archive with age estimates from this work. Points are scaled with planet radius and color-coded by planet equilibrium temperature. Ages have not been filtered for binarity nor corrected for metallicity.

(STScI). Funding for the Kepler mission is provided by the NASA Science Mission Directorate. STScI is operated by the Association of Universities for Research in Astronomy, Inc., under NASA contract NAS 5-26555. This paper makes use of data from the MEarth Project, which is a collaboration between Harvard University and the Smithsonian Astrophysical Observatory. The MEarth Project acknowledges funding from the David and Lucile Packard Fellowship for Science and Engineering and the National Science Foundation under grants AST-0807690, AST-1109468, and AST-1004488 (Alan T. Waterman Award), and a grant from the John Templeton Foundation.

## DATA AVAILABILITY

All data used in this work are in the public domain and available through various archives.

## REFERENCES

Adams F. C., Bodenheimer P., Laughlin G., 2005, *Astronomische Nachrichten*, **326**, 913

Agüeros M. A., et al., 2018, *ApJ*, **862**, 33

Alzate J. A., Bruzual G., Díaz-González D. J., 2021, *MNRAS*, **501**, 302

Amado P. J., et al., 2021, *A&A*, **650**, A188

Angus R., Morton T., Aigrain S., Foreman-Mackey D., Rajpaul V., 2018, *MNRAS*, **474**, 2094

Astudillo-Defru N., et al., 2017a, *A&A*, **602**, A88

Astudillo-Defru N., et al., 2017b, *A&A*, **605**, L11

Bakos G., Noyes R. W., Kovács G., Stanek K. Z., Sasselov D. D., Domša I., 2004, *PASP*, **116**, 266

Balona L. A., Abedigamba O. P., 2016, *MNRAS*, **461**, 497

Barnes S. A., 2007, *ApJ*, **669**, 1167

Basri G., Streichenberger T., McWard C., Edmond Lawrence I., Tan J., Lee M., Melton T., 2022, *ApJ*, **924**, 31

Batalha N. M., et al., 2013, *ApJS*, **204**, 24

Belokurov V., et al., 2020, *MNRAS*, **496**, 1922

Berger T. A., Huber D., van Saders J. L., Gaidos E., Tayar J., Kraus A. L., 2020, *AJ*, **159**, 280

Berta Z. K., Irwin J., Charbonneau D., Burke C. J., Falco E. E., 2012, *AJ*, **144**, 145

Biddle L. I., et al., 2014, *MNRAS*, **443**, 1810

Binks A. S., Jeffries R. D., 2014, *MNRAS*, **438**, L11

Borucki W. J., et al., 2010, *Science*, **327**, 977

Boulade O., 1998, *Experimental Astronomy*, **8**, 25

Boyajian T. S., et al., 2012, *ApJ*, **757**, 112

Bragaglia A., Fu X., Mucciarelli A., Andreuzzi G., Donati P., 2018, *A&A*, **619**, A176

Brandt T. D., 2021, *ApJS*, **254**, 42

Brown T. M., et al., 2013, *PASP*, **125**, 1031

Burke C. J., et al., 2014, *ApJS*, **210**, 19

Burt J., Vogt S. S., Butler R. P., Hanson R., Meschiari S., Rivera E. J., Henry G. W., Laughlin G., 2014, *ApJ*, **789**, 114

Caballero J. A., et al., 2022, *A&A*, **665**, A120

Canto Martins B. L., et al., 2020, *ApJS*, **250**, 20

Casali G., et al., 2020, *A&A*, **639**, A127

Charbonneau D., et al., 2009, *Nature*, **462**, 891

Christensen-Dalsgaard J., Aguirre V. S., 2018, in Deeg H. J., Belmonte J. A., eds., *Handbook of Exoplanets*. Springer, p. 184, doi:10.1007/978-3-319-55333-7\_184

Christy C. T., et al., 2022, arXiv e-prints, p. arXiv:2205.02239

Cieza L. A., et al., 2009, *ApJ*, **696**, L84

Clark C. A., van Belle G. T., Ciardi D. R., Lund M. B., Howell S. B., Everett M. E., Beichman C. A., Winters J. G., 2022, *AJ*, **163**, 232

Claytor Z. R., van Saders J. L., Santos Á. R. G., García R. A., Mathur S., Tayar J., Pinsonneault M. H., Shetrone M., 2020a, *kiauhoku: Stellar model grid interpolation, Astrophysics Source Code Library*, record ascl:2011.027 (ascl:2011.027)

Claytor Z. R., van Saders J. L., Santos Á. R. G., García R. A., Mathur S., Tayar J., Pinsonneault M. H., Shetrone M., 2020b, *ApJ*, **888**, 43

Claytor Z. R., van Saders J. L., Llama J., Sadowski P., Quach B., Avallone E. A., 2022, *ApJ*, **927**, 219

Cloutier R., Doyon R., Menou K., Delfosse X., Dumusque X., Artigau É., 2017, *AJ*, **153**, 9

Cody A. M., Hillenbrand L. A., 2010, *ApJS*, **191**, 389

Colomé J., Casteels K., Ribas I., Francisco X., 2010, in Radziwill N. M., Bridger A., eds, *Society of Photo-Optical Instrumentation Engineers (SPIE) Conference Series* Vol. 7740, *Software and Cyberinfrastructure for Astronomy*. p. 77403K, doi:10.1117/12.857672

Coughlin J. L., et al., 2016, *ApJS*, **224**, 12

Cukanovaitė E., Tremblay P. E., Toonen S., Temmink K. D., Manser C. J., O'Brien M. W., McCleery J., 2022, arXiv e-prints, p. arXiv:2209.13919

Cummings J. D., Deliyannis C. P., Maderak R. M., Steinhauer A., 2017, *AJ*, **153**, 128

Cunha D., Figueira P., Santos N. C., Lovis C., Boué G., 2013, *A&A*, **550**, A75

Curtis J. L., Wolfgang A., Wright J. T., Brewer J. M., Johnson J. A., 2013, *AJ*, **145**, 134

Curtis J. L., Agüeros M. A., Mamajek E. E., Wright J. T., Cummings J. D., 2019a, arXiv e-prints, p. arXiv:1905.10588

Curtis J. L., Agüeros M. A., Douglas S. T., Meibom S., 2019b, *ApJ*, **879**, 49

Curtis J. L., et al., 2020, *ApJ*, **904**, 140

David T. J., et al., 2018, *AJ*, **156**, 302

Dedrick C. M., et al., 2021, *AJ*, **161**, 86

Denissenkov P. A., Pinsonneault M., Terndrup D. M., Newsham G., 2010, *ApJ*, **716**, 1269

Díaz M. R., et al., 2019, arXiv e-prints, p. arXiv:1911.02012

Díez Alonso E., et al., 2019, *MNRAS*, **489**, 5928

Distefano E., et al., 2022, arXiv e-prints, p. arXiv:2206.05500

Donati J. F., et al., 2020, *MNRAS*, **498**, 5684

Dotter A., Chaboyer B., Jevremović D., Kostov V., Baron E., Ferguson J. W., 2008, *ApJS*, **178**, 89

Douglas S. T., Curtis J. L., Agüeros M. A., Cargile P. A., Brewer J. M., Meibom S., Jansen T., 2019, *ApJ*, **879**, 100

Dungee R., 2022, PhD thesis, University of Hawaii at Manoa

Dungee R., van Saders J., Gaidos E., Chun M., García R. A., Magnier E. A., Mathur S., Santos Á. R. G., 2022, *ApJ*, **938**, 118

El-Badry K., Rix H.-W., Heintz T. M., 2021, *MNRAS*, **506**, 2269

Epstein C. R., Pinsonneault M. H., 2014, *ApJ*, **780**, 159

Esselein R., Aigrain S., Vanderburg A., Smith J. C., Meibom S., Van Saders J., Mathieu R., 2018, *ApJ*, **859**, 167

Feiden G. A., 2016, *A&A*, **593**, A99

Feng F., et al., 2019, *ApJS*, **242**, 25

Fleming D. P., Barnes R., Davenport J. R. A., Luger R., 2019, *ApJ*, **881**, 88

Foster G., Poppenhaeger K., Ilic N., Schworer A., 2022, *A&A*, **661**, A23

Fragkou V., Parker Q. A., Zijlstra A. A., Vázquez R., Sabin L., Rechy-Garcia J. S., 2022, *ApJ*, **935**, L35

Fritzewski D. J., Barnes S. A., James D. J., Strassmeier K. G., 2020, *A&A*, **641**, A51

Fu X., et al., 2022, arXiv e-prints, p. [arXiv:2207.09121](https://arxiv.org/abs/2207.09121)

Gaia Collaboration et al., 2016, *A&A*, **595**, A1

Gaia Collaboration et al., 2022, arXiv e-prints, p. [arXiv:2208.00211](https://arxiv.org/abs/2208.00211)

Gaidos E., Mann A. W., Kraus A. L., Ireland M., 2016, *MNRAS*, **457**, 2877

Gallet F., Bouvier J., 2015, *A&A*, **577**, A98

Gan T., et al., 2020, *AJ*, **159**, 160

Giacobbe P., et al., 2020, *MNRAS*, **491**, 5216

Gizis J. E., 1997, *AJ*, **113**, 806

Godoy-Rivera D., Pinsonneault M. H., Rebull L. M., 2021, *ApJS*, **257**, 46

González-Álvarez E., et al., 2021, *A&A*, **649**, A157

Gossage S., Conroy C., Dotter A., Choi J., Rosenfield P., Cargile P., Dolphin A., 2018, *ApJ*, **863**, 67

Hambleton K. M., et al., 2022, arXiv e-prints, p. [arXiv:2208.04499](https://arxiv.org/abs/2208.04499)

Hardegree-Ullman K. K., Cushing M. C., Muirhead P. S., Christiansen J. L., 2019, *AJ*, **158**, 75

Hartman J. D., Bakos G. Á., Noyes R. W., Sipócz B., Kovács G., Mazeh T., Shporer A., Pál A., 2011, *AJ*, **141**, 166

Hedges C., Angus R., Barentsen G., Saunders N., Montet B. T., Gully-Santiago M., 2020, *Research Notes of the American Astronomical Society*, **4**, 220

Heiter U., Soubiran C., Netopil M., Paunzen E., 2014, *A&A*, **561**, A93

Helled R., Morbidelli A., 2021, in Madhusudhan N., ed., , *ExoFrontiers: Big Questions in Exoplanetary Science*. Institute of Physics, pp 12–1, doi:10.1088/2514-3433/abfa8fch12

Henry G. W., 1999, *PASP*, **111**, 845

Howard A. W., et al., 2014, *ApJ*, **794**, 51

Howell S. B., et al., 2014, *PASP*, **126**, 398

Hsu D. C., Ford E. B., Ragozzine D., Ashby K., 2019, *AJ*, **158**, 109

Huber D., et al., 2016, *ApJS*, **224**, 2

Isern J., 2019, *ApJ*, **878**, L11

Jeffries R. D., Jackson R. J., Briggs K. R., Evans P. A., Pye J. P., 2011, *MNRAS*, **411**, 2099

Kane S. R., von Braun K., Henry G. W., Waters M. A., Boyajian T. S., Mann A. W., 2017, *ApJ*, **835**, 200

Kemmer J., et al., 2020, *A&A*, **642**, A236

Kemmer J., et al., 2022, *A&A*, **659**, A17

Kilic M., Munn J. A., Harris H. C., von Hippel T., Liebert J. W., Williams K. A., Jeffery E., DeGennaro S., 2017, *ApJ*, **837**, 162

Kiraga M., Stepien K., 2007, *Acta Astron.*, **57**, 149

Kite E. S., Manga M., Gaidos E., 2009, *ApJ*, **700**, 1732

Kochanek C. S., et al., 2017, *PASP*, **129**, 104502

Kounkel M., et al., 2019, *AJ*, **157**, 196

Kounkel M., Stassun K. G., Bouma L. G., Covey K., Hillenbrand L. A., Lee Curtis J., 2022, *AJ*, **164**, 137

Kraus A. L., Ireland M. J., Hillenbrand L. A., Martinache F., 2012, *ApJ*, **745**, 19

Kraus A. L., Ireland M. J., Huber D., Mann A. W., Dupuy T. J., 2016, *AJ*, **152**, 8

Lam K. W. F., et al., 2021, *Science*, **374**, 1271

Lamman C., et al., 2020, *AJ*, **159**, 139

Lammer H., 2013, *Origin and Evolution of Planetary Atmospheres*. Springer, doi:10.1007/978-3-642-32087-3

Lépine S., Shara M. M., 2005, *AJ*, **129**, 1483

Lothringer J. D., et al., 2018, *AJ*, **155**, 66

Lu Y., Curtis J. L., Angus R., David T. J., Hattori S., 2022, arXiv e-prints, p. [arXiv:2210.06604](https://arxiv.org/abs/2210.06604)

Lubin J., et al., 2021, arXiv e-prints, p. [arXiv:2105.07005](https://arxiv.org/abs/2105.07005)

Luque R., et al., 2018, *A&A*, **620**, A171

Luque R., et al., 2019, *A&A*, **628**, A39

Magaudda E., Stelzer B., Covey K. R., Raetz S., Matt S. P., Scholz A., 2020, *A&A*, **638**, A20

Maldonado J., et al., 2021, *A&A*, **651**, A93

Mallonn M., et al., 2018, *A&A*, **614**, A35

Mann A. W., Brewer J. M., Gaidos E., Lépine S., Hilton E. J., 2013, *AJ*, **145**, 52

Mann A. W., Deacon N. R., Gaidos E., Ansdel M., Brewer J. M., Liu M. C., Magnier E. A., Aller K. M., 2014, *AJ*, **147**, 160

Mann A. W., Feiden G. A., Gaidos E., Boyajian T., von Braun K., 2015, *ApJ*, **804**, 64

Mann A. W., et al., 2019, *ApJ*, **871**, 63

Masci F. J., et al., 2019, *PASP*, **131**, 018003

Matt S. P., Pinzón G., Greene T. P., Pudritz R. E., 2012, *ApJ*, **745**, 101

Matt S. P., Brun A. S., Baraffe I., Bouvier J., Chabrier G., 2015, *ApJ*, **799**, L23

Messina S., 2019, *A&A*, **627**, A97

Miyakawa K., Hirano T., Sato B., Okuzumi S., Gaidos E., 2022, *AJ*, **164**, 209

Molenda-Żakowicz J., Brogaard K., Niemczura E., Bergemann M., Frasca A., Arentoft T., Grundahl F., 2014, *MNRAS*, **445**, 2446

Montes D., et al., 2018, *MNRAS*, **479**, 1332

Mor R., Robin A. C., Figueras F., Roca-Fàbregas S., Luri X., 2019, *A&A*, **624**, L1

Morris B. M., 2020, *ApJ*, **893**, 67

Mulders G. D., Pascucci I., Apai D., 2015, *ApJ*, **798**, 112

Mullally F., et al., 2015, *ApJS*, **217**, 31

Nakajima T., Oppenheimer B. R., Kulkarni S. R., Golimowski D. A., Matthews K., Durrance S. T., 1995, *Nature*, **378**, 463

Newton E. R., Mondrik N., Irwin J., Winters J. G., Charbonneau D., 2018, *AJ*, **156**, 217

Nicholson B. A., Aigrain S., 2022, *MNRAS*, **515**, 5251

Oelkers R. J., et al., 2018, *AJ*, **155**, 39

Otani T., von Hippel T., Buzasi D., Oswalt T. D., Stone-Martinez A., Majewski P., 2022, *ApJ*, **930**, 36

Pasquini L., Biazzo K., Bonifacio P., Randich S., Bedin L. R., 2008, *A&A*, **489**, 677

Passegger V. M., et al., 2022, *A&A*, **658**, A194

Pecaut M. J., Mamajek E. E., 2013, *ApJS*, **208**, 9

Pepe F., et al., 2000, in Iye M., Moorwood A. F., eds, *Society of Photo-Optical Instrumentation Engineers (SPIE) Conference Series Vol. 4008, Optical and IR Telescope Instrumentation and Detectors*. pp 582–592, doi:10.1117/12.395516

Pepe F., et al., 2021, *A&A*, **645**, A96

Pojmanski G., 2002, *Acta Astron.*, **52**, 397

Pollacco D. L., et al., 2006, *PASP*, **118**, 1407

Quirrenbach A., et al., 2016, *CARMENES: an overview six months after first light*. SPIE, p. 990812, doi:10.1117/12.2231880

Rebassa-Mansergas A., et al., 2021, *MNRAS*, **505**, 3165

Rebull L. M., et al., 2016, *AJ*, **152**, 113

Rebull L. M., Stauffer J. R., Cody A. M., Hillenbrand L. A., David T. J., Pinsonneault M., 2018, *AJ*, **155**, 196

Reefe M. A., et al., 2022, *AJ*, **163**, 269

Reiners A., et al., 2018, *A&A*, **609**, L5

Reinhold T., Hekker S., 2020, *A&A*, **635**, A43

Reinhold T., Reiners A., Basri G., 2013, *A&A*, **560**, A4

Reipurth B., Mikkola S., 2012, *Nature*, **492**, 221

Ribas I., et al., 2018, *Nature*, **563**, 365

Richer H. B., Fahlman G. G., Rosvick J., Ibata R., 1998, *ApJ*, **504**, L91

Ricker G. R., et al., 2014, in *Proc. SPIE*. p. 914320 (arXiv:1406.0151), doi:10.1117/12.2063489

Rigault M., 2018, *ztfquery*, a Python tool to access ZTF data, Zenodo, doi:10.5281/zenodo.1345222

Rigaut F., 2002, in *European Southern Observatory Conference and Workshop Proceedings*. p. 11

Robertson P., Mahadevan S., Endl M., Roy A., 2014, *Science*, **345**, 440

Rodríguez-López C., 2019, *Frontiers in Astronomy and Space Sciences*, **6**, 76

Roquette J., Matt S. P., Winter A. J., Amard L., Stasevic S., 2021, *MNRAS*, **508**, 3710

Rosotti G. P., Clarke C. J., 2018, *MNRAS*, **473**, 5630

Rowe J. F., et al., 2015, *ApJS*, **217**, 16

Sanchis-Ojeda R., et al., 2015, *ApJ*, **812**, 112

Sandquist E. L., et al., 2021, *AJ*, **161**, 59

Santos A. R. G., García R. A., Mathur S., Bugnet L., van Saders J. L., Metcalfe T. S., Simonian G. V. A., Pinsonneault M. H., 2019, *ApJS*, **244**, 21

Santos A. R. G., Breton S. N., Mathur S., García R. A., 2021, *ApJS*, **255**, 17

Sarajedini A., Dotter A., Kirkpatrick A., 2009, *ApJ*, **698**, 1872

Scargle J. D., 1982, *ApJ*, **263**, 835

Schiavon R. P., Caldwell N., Rose J. A., 2004, *AJ*, **127**, 1513

Serna J., et al., 2021, *ApJ*, **923**, 177

Shappee B. J., et al., 2014, *ApJ*, **788**, 48

Shporer A., et al., 2020, *ApJ*, **890**, L7

Simonian G. V. A., Pinsonneault M. H., Terndrup D. M., 2019, *ApJ*, **871**, 174

Skumanich A., 1972, *ApJ*, **171**, 565

Somers G., Stauffer J., Rebull L., Cody A. M., Pinsonneault M., 2017, *ApJ*, **850**, 134

Souto D., et al., 2020, *ApJ*, **890**, 133

Sozzetti A., et al., 2013, in European Physical Journal Web of Conferences. p. 03006 ([arXiv:1303.1275](https://arxiv.org/abs/1303.1275)), doi:10.1051/epjconf/20134703006

Stauffer J., et al., 2016, *AJ*, **152**, 115

Stock S., et al., 2020, *A&A*, **643**, A112

Strassmeier K. G., et al., 2004, *Astronomische Nachrichten*, **325**, 527

Su X.-N., Xie J.-W., Zhou J.-L., Thebault P., 2021, *AJ*, **162**, 272

Suárez Mascareño A., Rebolo R., González Hernández J. I., Esposito M., 2015, *MNRAS*, **452**, 2745

Suárez Mascareño A., Rebolo R., González Hernández J. I., 2016, *A&A*, **595**, A12

Suárez Mascareño A., Rebolo R., González Hernández J. I., Esposito M., 2017, *MNRAS*, **468**, 4772

Suárez Mascareño A., et al., 2018, *A&A*, **612**, A89

Suto Y., Sasaki S., Nakagawa Y., Benomar O., 2022, *PASJ*, **74**, 857

Terrien R. C., et al., 2022, *ApJ*, **927**, L11

Thompson S. E., et al., 2018, *ApJS*, **235**, 38

Toledo-Padrón B., et al., 2019, *MNRAS*, **488**, 5145

Toledo-Padrón B., et al., 2021, *A&A*, **648**, A20

Toyouchi D., Chiba M., 2018, *ApJ*, **855**, 104

VandenBerg D. A., Stetson P. B., 2004, *PASP*, **116**, 997

VanderPlas J. T., 2018, *ApJS*, **236**, 16

Venuti L., et al., 2017, *A&A*, **599**, A23

Walkowicz L. M., Basri G. S., 2013, *MNRAS*, **436**, 1883

Winters J. G., et al., 2019, *AJ*, **157**, 216

Woźniak P. R., et al., 2004, *AJ*, **127**, 2436

Wright N. J., Newton E. R., Williams P. K. G., Drake J. J., Yadav R. K., 2018, *MNRAS*, **479**, 2351

Xiang M., Rix H.-W., 2022, *Nature*, **603**, 599

Yang H., Liu J., 2019, *ApJS*, **241**, 29

Ziegler C., et al., 2018, *AJ*, **156**, 83

Ziegler C., Tokovinin A., Latiolais M., Briceño C., Law N., Mann A. W., 2021, *AJ*, **162**, 192

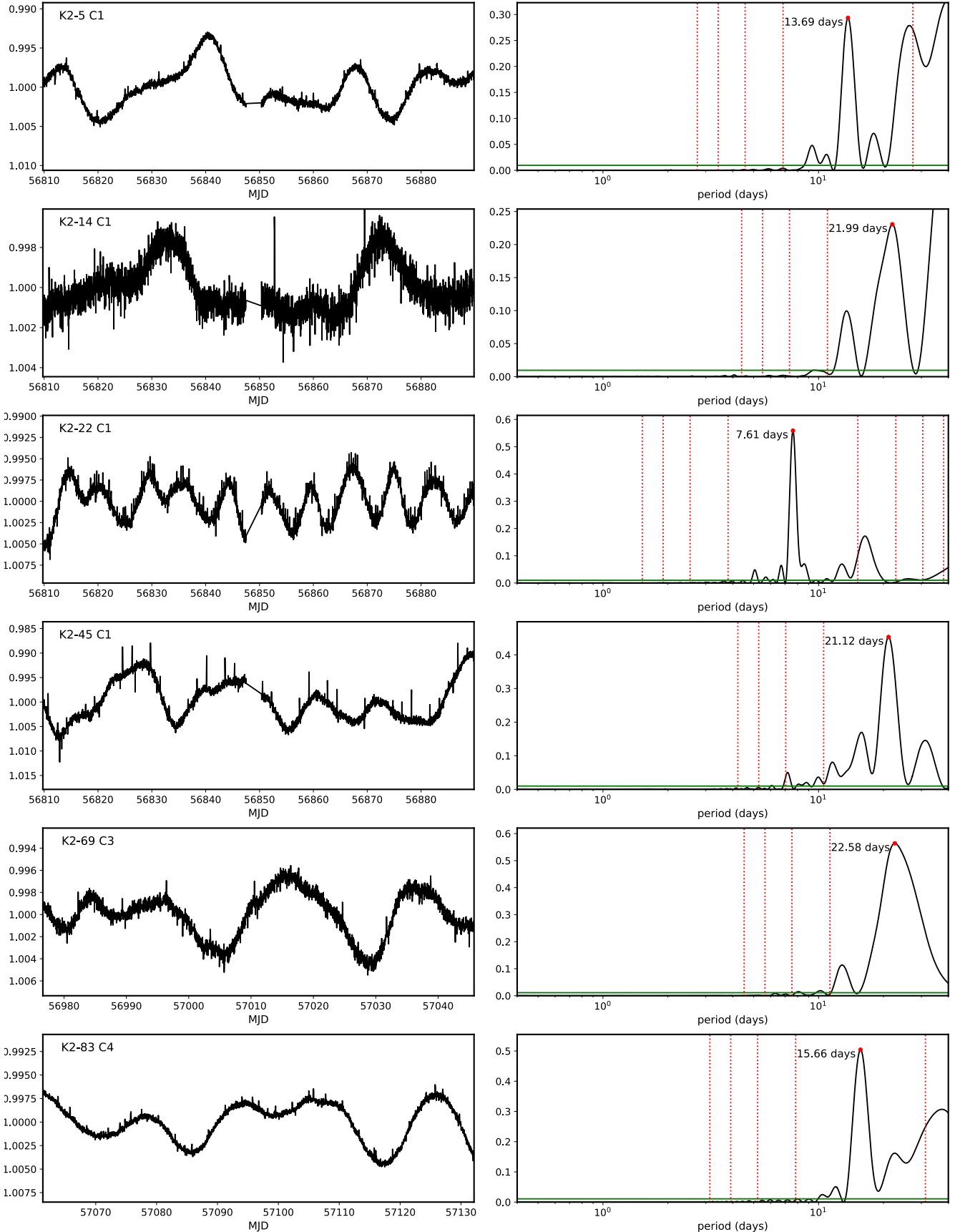
van Saders J. L., Pinsonneault M. H., 2013, *ApJ*, **776**, 67

## APPENDIX A: LIGHTCURVE ANALYSIS

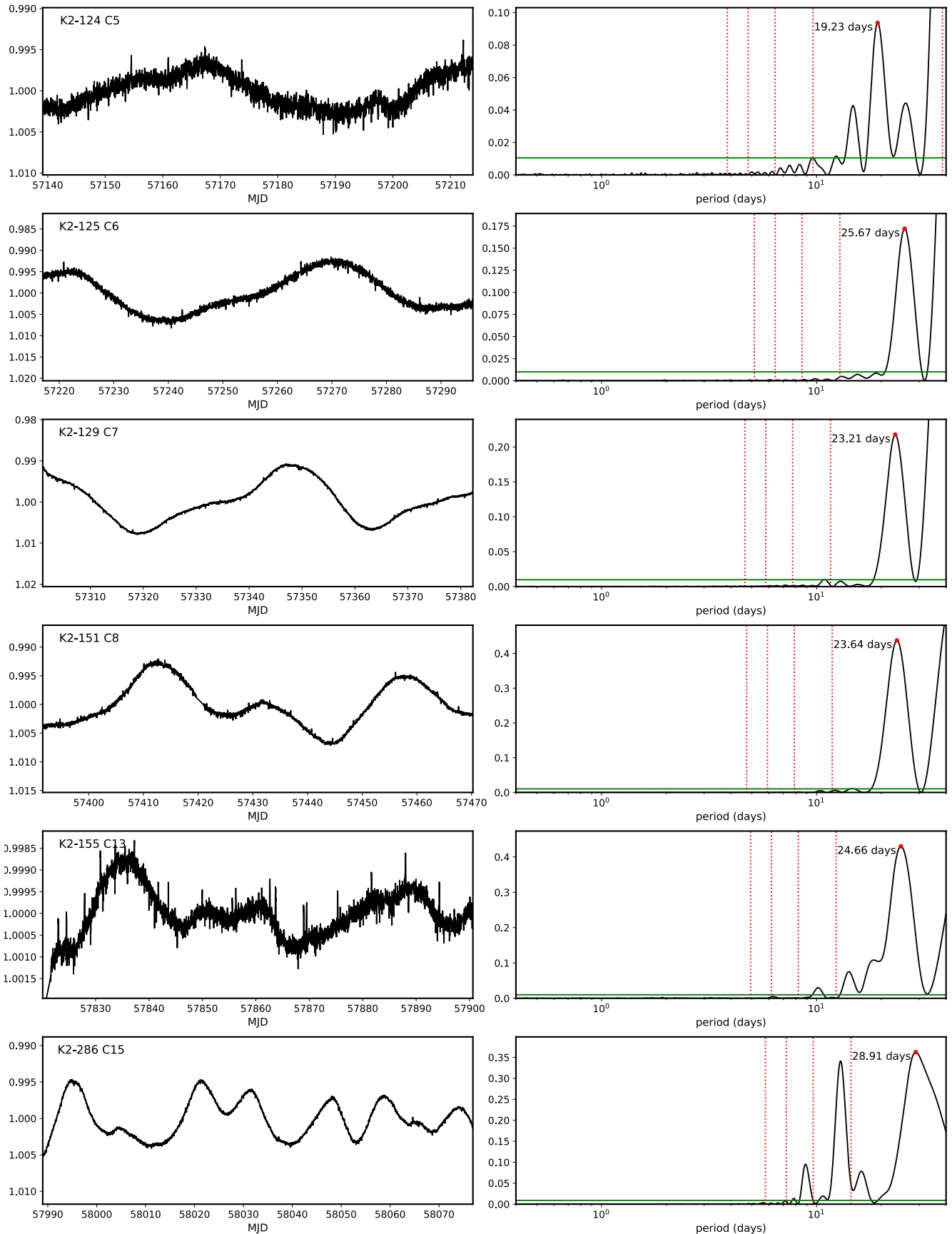
Figures A1-A4 show *K2* lightcurves of 21 host star in which new rotational signals were identified or, in the case of K2-345, replace a previously published value. In the cases of K2-5, 14, 83, 124, 125, 129, 151, 288 B, 315, 322, and 377, a rotation period twice the period of the signal with peak power was adopted. Figure A5 shows periodograms and phased lightcurves from ZTF photometry

of four host stars for which new rotation periods are identified and reported in this work. Fig. A6 shows the ASAS-SN data for four stars for which significant ( $p < 0.01$ ) signals with the same period appear in both *g*- and *V*-band photometry. In the case of GJ 486, the recovered signal at 13.7 days differs markedly from the value of  $49.9 \pm 5.5$  days published by Caballero et al. (2022).

This paper has been typeset from a *TeX/LaTeX* file prepared by the author.



**Figure A1.** De-trended *K2* PDCSAP lightcurves of M dwarf host stars with significant periodic signals. The left panels contain the lightcurves. The right panels show the Lomb-Scargle periodograms with the horizontal green line marking the false alarm probability  $p = 0.001$ , the red point marking the period of highest power, and the vertical dashed lines marking upper and lower harmonics of that period. For K2-22, twice the peak period was adopted.

**Figure A2.** Additional *K2* lightcurves. See Fig. A1 for explanation.

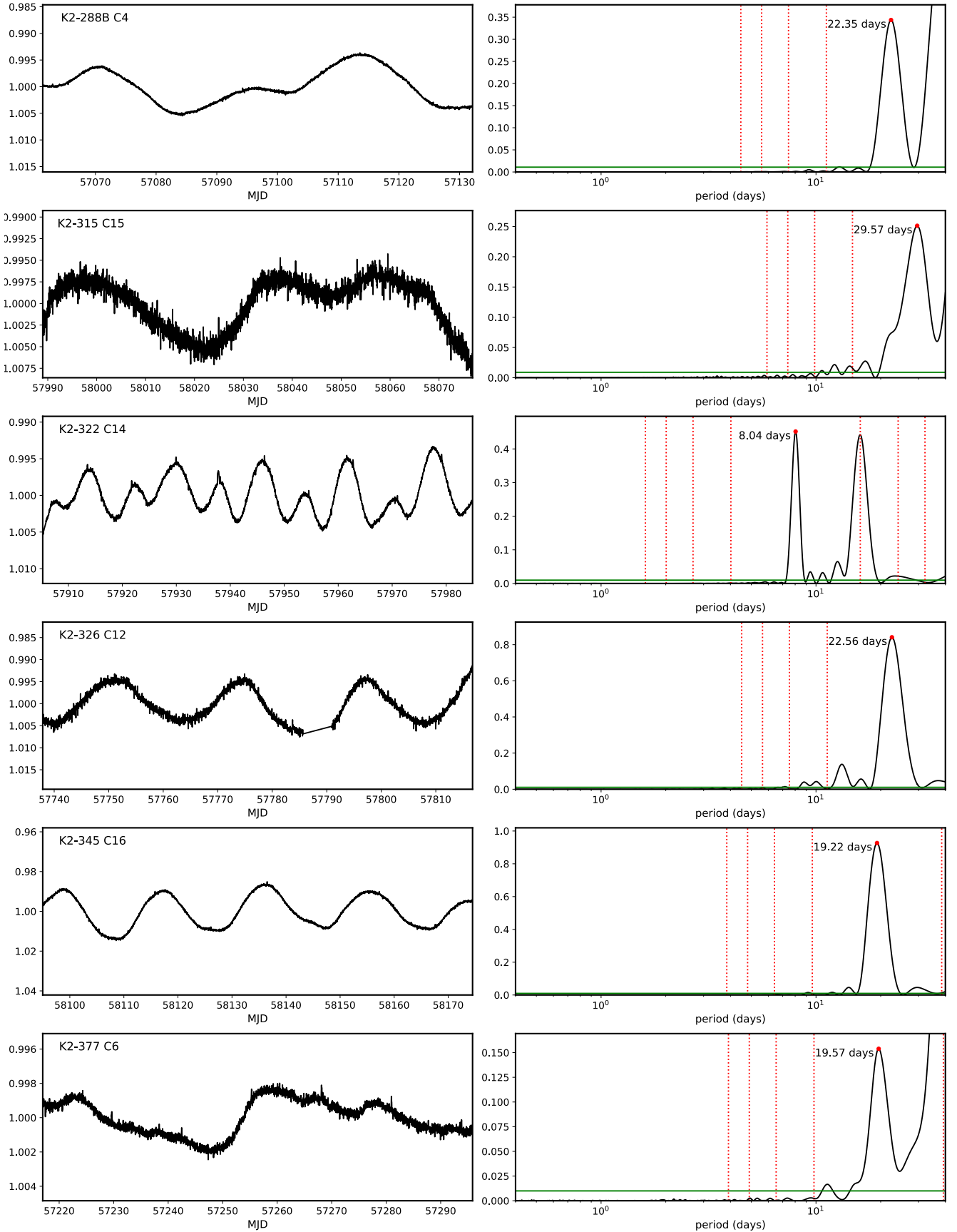


**Figure A3.** Additional K2 lightcurves. See Fig. A1 for explanation. For K2-322, twice the peak period was adopted.

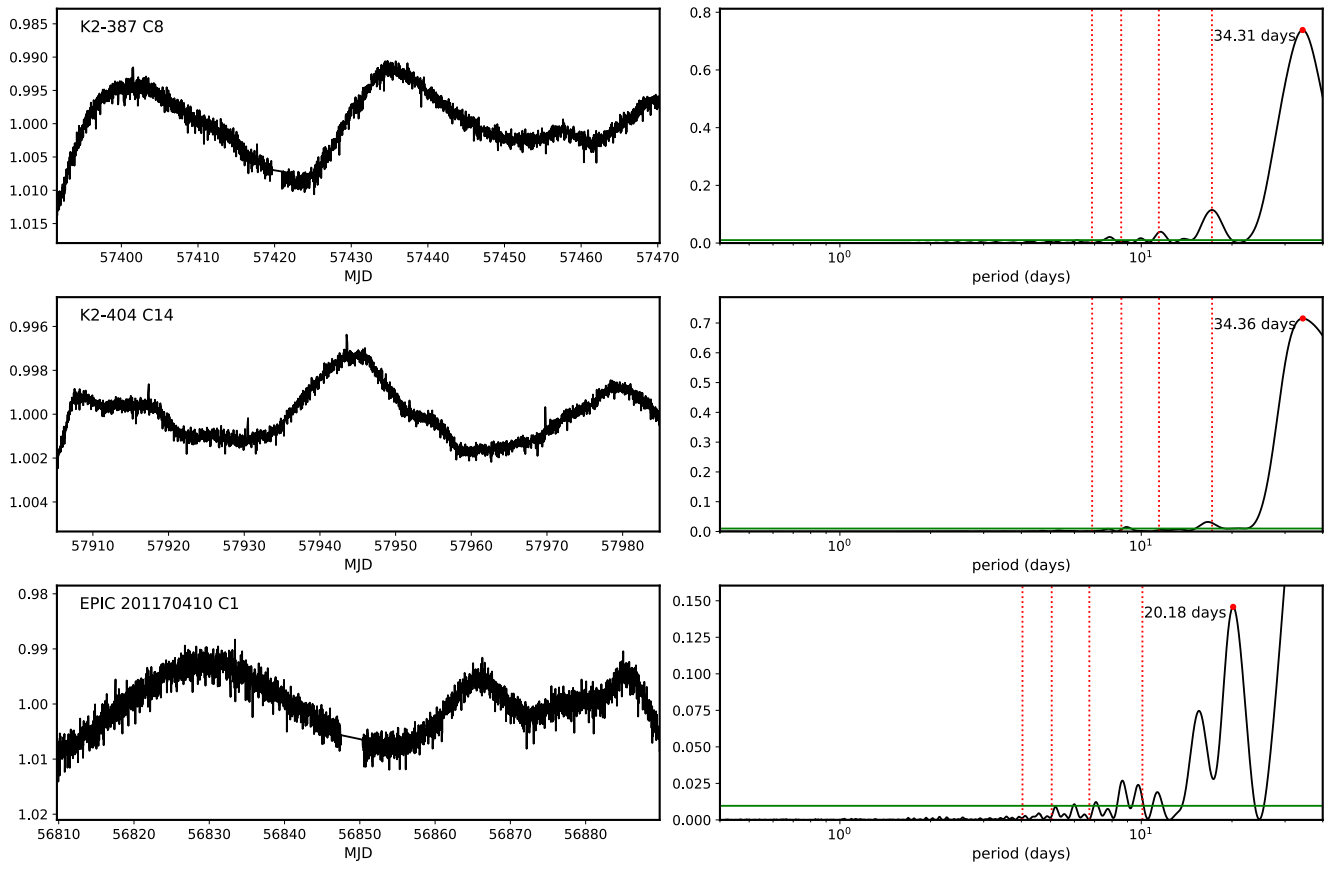


**Figure A4.** Additional *K2* lightcurves. See Fig. A1 for explanation.

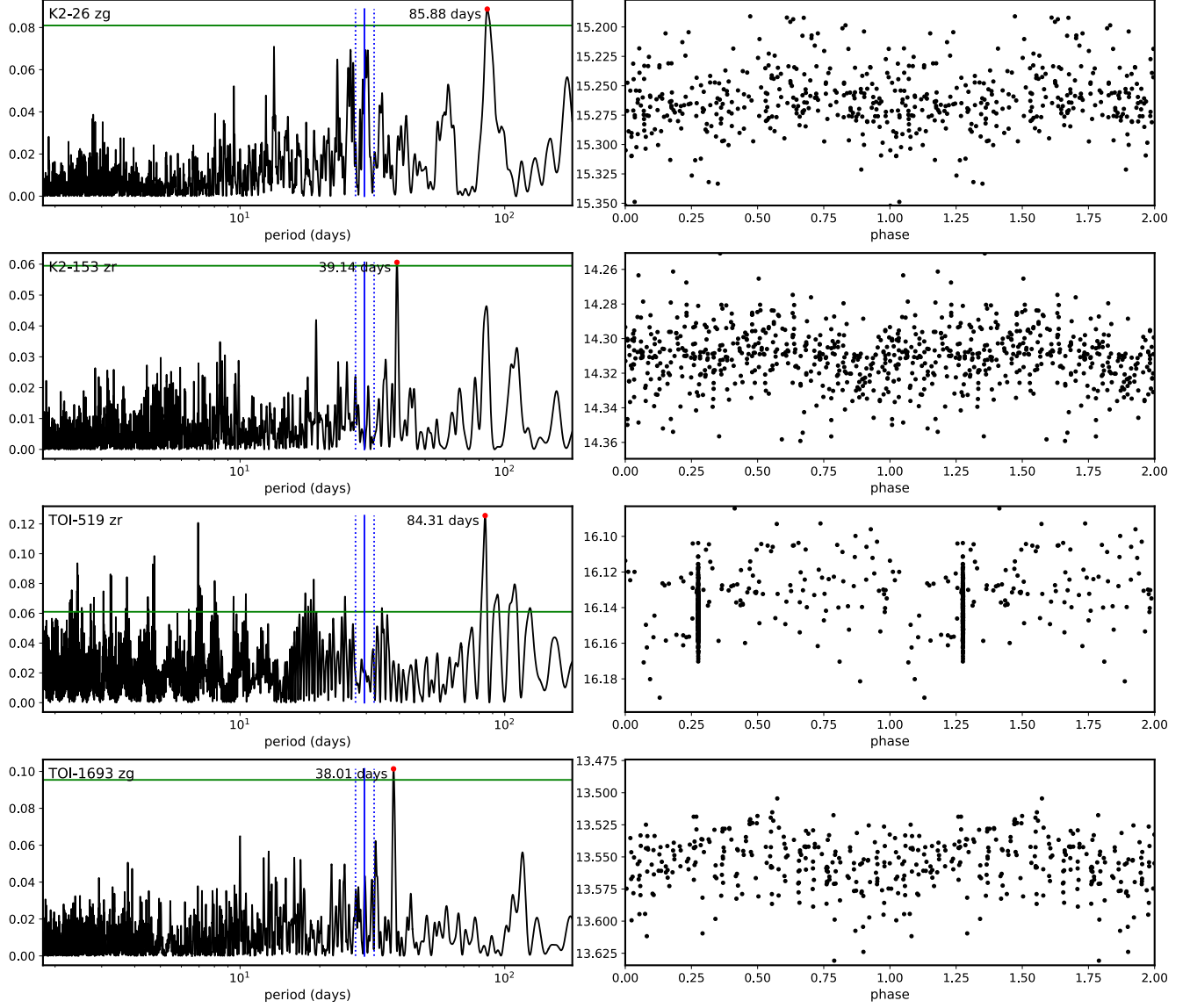


**Figure A5.** Periodograms and phased ZTF lightcurves of four M dwarf exoplanet hosts with significant ( $p < 0.01$ , horizontal green line) signals (red dots) that passed our visual inspection and are considered candidate rotational signals. The host star and the band-pass are indicated in the The blue solid and dashed lines are the lunar synodic period and its aliases with the annual observing window function. Note that the phased lightcurves are repeated.

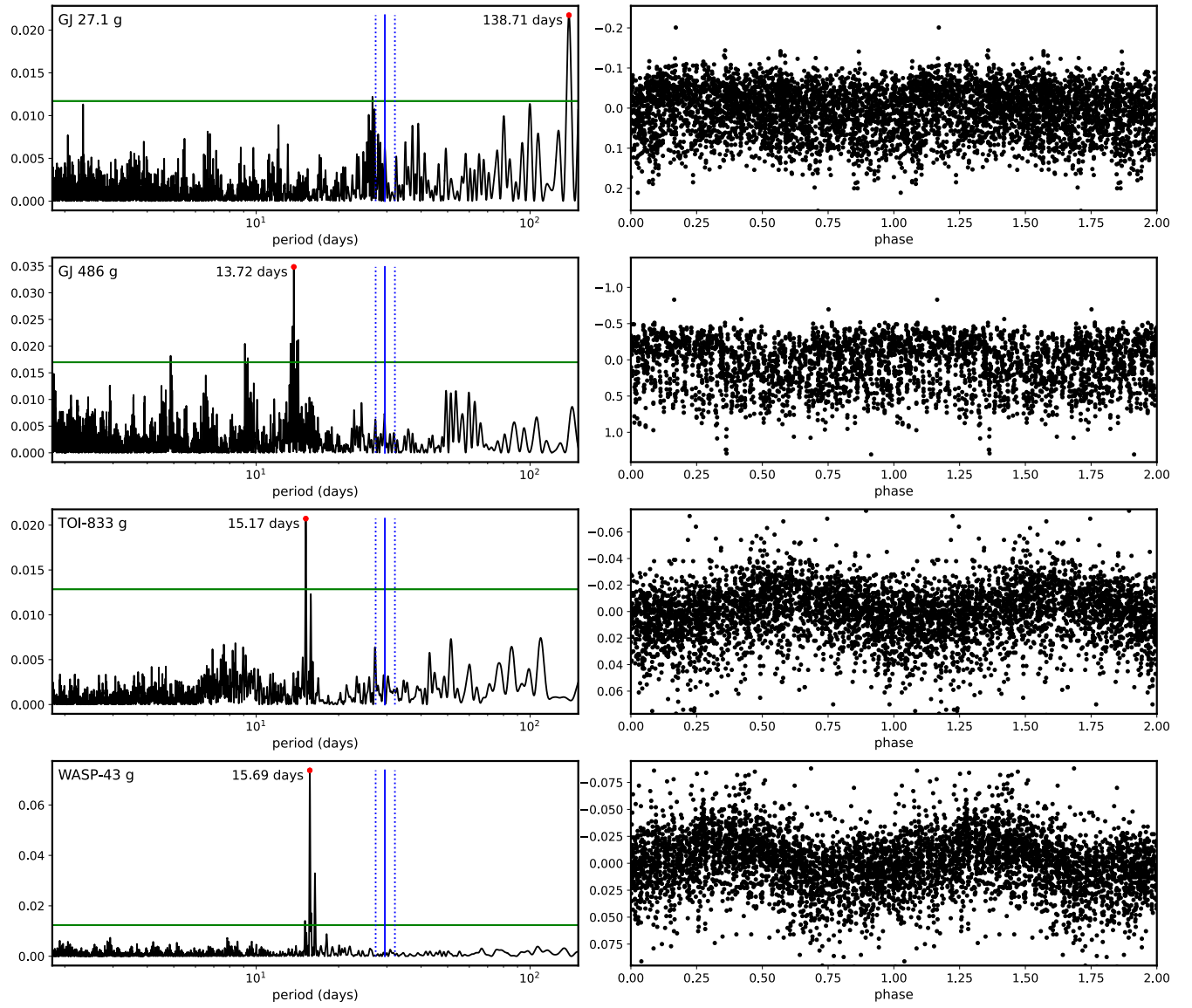


**Figure A6.** Periodograms and phased ASAS-SN g-band lightcurves of four M dwarf exoplanet hosts with significant ( $p < 0.01$ , horizontal green line) signals (red dots) that also had equivalent significant signals in V-band, passed our visual inspection, and are considered candidate rotational signals. The blue solid and dashed lines are the lunar synodic period and its aliases with the annual observing window function. Note that the phased lightcurves are repeated.